Doctor of Philosophy

STUDY ON LATTICE STRUCTURES USING ADDITIVE MANUFACTURING AND ITS APPLICATION ON CONFORMAL COOLING CHANNEL FOR HOT STAMPING

The Graduate School of the University of Ulsan

School of Mechanical Engineering

Van Loi Tran

July 2024

STUDY ON LATTICE STRUCTURES USING ADDITIVE MANUFACTURING AND ITS APPLICATION ON CONFORMAL COOLING CHANNEL FOR HOT STAMPING

Advisor: **Sung-Tae Hong**

A Dissertation

Submitted to the Graduate School of the University of Ulsan

in Partial Fulfillment of the Requirements

for the Degree of

Doctor of Philosophy

by

Van Loi Tran

School of Mechanical Engineering

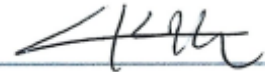University of Ulsan, Ulsan, Korea

July 2024

STUDY ON LATTICE STRUCTURES USING ADDITIVE

MANUFACTURING AND ITS APPLICATION ON

CONFORMAL COOLING CHANNEL FOR HOT STAMPING

This certifies that the dissertation of

Van Loi Tran is approved by

Committee Chairman:	Prof. Doo-Man Chun	
Committee Member:	Prof. Sung-Tae Hong	
Committee Member:	Prof. Koo-Hyun Chung	
Committee Member:	Prof. Namhun Kim	
Committee Member:	Dr. Dong-Hyun Kim	
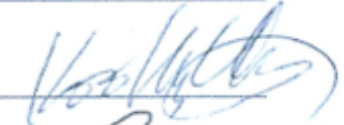
School of Mechanical Engineering

University of Ulsan, Korea

July 2024

Van Loi Tran 의

공학박사 학위 논문을 인준함

심사위원	천두만	인
심사위원	홍성태	인
심사위원	정구현	인
심사위원	김남훈	인
심사위원	김동현	인

울 산 대 학 교 대 학 원

기계자동차공학과

2024 년 07월

ACKNOWLEDGMENTS

First, I would like to express my deepest gratitude to my advisor – Prof. Sung-Tae Hong for his guidance, assistance, encouragement, and insightful suggestions which have been invaluable to the development of my ideas for both my papers and my life. Prof. Sung-Tae Hong has taught me to think deeply and critically in research, helping me reach the level of a doctoral candidate. This work would not have been possible without his assistance. I cannot find adequate words to express my gratitude for your kindness and support.

I particularly want to thank my second advisor – Dr. Dong-Huyn Kim, for his invaluable advice, support, and guidance. I would like to thank all staff from the Korea Institute of Industrial Technology (KITECH) for their support and valuable discussions during my studies. I wish to express my appreciation to all Advanced Engineering Materials Lab colleagues for their help in my research and experiments. I also thank all those who have helped me in one way or another during my Ph. D period.

Finally, I am incredibly grateful to my wife – Doan Thi Xuan Loan, my parents for their continuous encouragement, understanding, and support.

Van Loi Tran

i

TABLE OF CONTENT

LIST OF FIGURES

LIST OF TABLES

올산대학교
UNIVERSITY OF ULSAN

CHAPTER I

INTRODUCTION

In the rapidly evolving field of engineering and industry, the introduction of additive manufacturing (AM), often known as 3D printing, stands out as a game-changing technology [1]. Unlike traditional manufacturing technologies such as casting or machining, AM manufactures products layer by layer, enabling the creation of previously unattainable and extremely complex geometries [2,3]. Design for Additive Manufacturing (DfAM) is a holistic design philosophy that takes advantage of the particular possibilities of AM technologies. Among the different AM applications, the design and fabrication of lattice structures have received a lot of interest due to their remarkable mechanical capabilities and lightweight attributes [4].

Lattice structures are open cellular frameworks made up of repeated unit cells that vary in size, shape, and topology. These structures have a high strength-to-weight ratio [6], lightweight, low thermal expansion coefficient [7], negative Poisson's ratio [8], high energy absorption [9], making them appropriate for applications that require weight reduction while maintaining mechanical performance. The introduction of additive manufacturing has dramatically improved the capacity to design and construct such complicated structures. Lattice structures can be designed to have certain mechanical qualities, such as stiffness, strength, and energy absorption, that are required for applications in aerospace [10], automotive [11], biomedical [12], and other high-tech industries.

Lattice structures for AM require numerous essential factors to guarantee good performance and manufacturability. The key parameters include [13]:

울산대학교
UNIVERSITY OF ULSAN

- Unit cell geometry: The shape and arrangement of unit cells (cubic, tetrahedral, octahedral) affect the mechanical properties of the lattice. Designers must select the suitable cell geometry depending on the planned application and performance specifications.

- Unit cell size and density: Strut thickness and lattice density affect the structure's weight and strength. Fine-tuning these parameters is critical for achieving the ideal balance of weight reduction and mechanical integrity.

- Topology optimization: Computational tools and algorithms can optimize lattice structures to improve mechanical performance and reduce material utilization. Topology optimization determines the most efficient material distribution inside a particular volume.

In addition to design considerations, the study investigates the complexities of additive manufacturing methods and their impact on lattice structure construction. Various AM technologies, including as selective laser sintering (SLS) [14], stereolithography (SLA) [15], fused deposition modeling (FDM) [16], and electron beam melting (EBM) [17], have different advantages and disadvantages in terms of resolution, material compatibility, and build speed. Understanding the relationship between AM parameters such layer thickness, scanning speed, and build orientation is critical for getting the best lattice structure quality and mechanical performance [18].

Material selection is another important component of the study, as the mechanical properties and behavior of lattice structures are inextricably linked to the qualities of the materials utilized [19,20]. From polymers [21] and metals [22] to ceramics and composites, AM techniques may use a wide range of materials to create lattice structures with specific features. The study assesses the

mechanical behavior, thermal characteristics, and biocompatibility of several AM-compatible materials, providing information on material selection criteria for specific applications.

Furthermore, the study looks at the mechanical behavior of lattice systems under various loading circumstances, including tension, compression, bending, and fatigue. Engineers can use experimental testing and finite element analysis (FEA) to accurately examine the structural performance, stiffness, strength, and failure processes of lattice systems [23,24]. The goal of this study is to create strong guidelines for the optimal design and fabrication of lattice structures across many engineering disciplines by explaining the complicated interaction between design parameters, manufacturing processes, and material properties.

In the present study, chapter II serves as an introduction to the fundamental definitions, principles, and evolution of various additive manufacturing (AM) processes. It delineates the general procedures for materializing physical components from digital 3D design data, and categorizes AM processes while elucidating the principles underpinning each category. Furthermore, it delves into AM applications in metal forming, including material selection, structural optimization, and conformal cooling systems.

Chapter III experimentally examines the influence of base materials, including stainless steel 316L, tool steel 1.2709, titanium alloy (Ti-Gr.2), and aluminum alloy (AlSi10Mg), on the mechanical properties of additively manufactured (AMed) FCCXYZ lattice structures. The lattice structures, with relative density (RD) ranging from 0.11 to 0.36, exhibit diverse compressive failure modes contingent on their RD. The observed failure modes include a layer-by-layer collapse mode at low RD and a bulk failure mode at high RD. Furthermore, a Gibson-Ashby model is developed to provide an accurate prediction of the performance of FCCXYZ lattice structures

3

across varying RDs. The findings from this research provide valuable insights for the design of energy-absorbing components in metal additive manufacturing.

In chapter IV, the design principle of an additively manufactured (AMed) lattice structural conformal cooling channel for hot stamping is investigated. AM with selective laser melting is adopted to fabricate a lab-scale rapid cooling die filled with conformal lattice structures, which provide structural stiffness, act as thermal fins, and expedite the occurrence of turbulent flow in the channel. Three different surface area densities with the same RD were considered to evaluate the heat transfer and cooling performance. Computational fluid dynamics is used to analyze the flow of coolant in the lattice structures with different surface area densities. The experimental and computational results show that if the surface density of the lattice structure is selected properly, the cooling performance can be enhanced significantly while maintaining a constant RD, which directly affects the weight reduction and stiffness of the cooling die.

References

[1]   Ataollahi, S. A review on additive manufacturing of lattice structures in tissue engineering. *Bioprinting* **35**, e00304 (2023).

[2]   Buchanan C, Gardner L. Metal 3D printing in construction: A review of methods, research, applications, opportunities and challenges. Eng Struct 2019;180:332–48.

[3]   Gibson I, Rosen D, Stucker B. Additive Manufacturing Technologies: 3D Printing, Rapid Prototyping, and Direct Digital Manufacturing. New York, NY: Springer New York; 2015.

[4]   Spalt P, Bauernhansl T. A Framework for Integration of Additive Manufacturing Technologies in Production Networks. Proc CIRP 2016;57:716–21.

[5]   Klahn C, Leutenecker B, Meboldt M. Design Strategies for the Process of Additive Manufacturing. Proc CIRP 2015;36:230–5.

[6]   Kelly, C. N. *et al.* Fatigue behavior of As-built selective laser melted titanium scaffolds with sheet-based gyroid microarchitecture for bone tissue engineering. *Acta Biomaterialia* **94**, 610–626 (2019).

[7]   Gibson LJ, Ashby MF. Cellular Solids: Structure and Properties. 2nd ed. Cambridge University Press; 1997.

[8]   Wei, K. *et al.* Three dimensional lightweight lattice structures with large positive, zero and negative thermal expansion. *Composite Structures* **188**, 287–296 (2018).

[9]   Yan, C., Hao, L., Hussein, A. & Raymont, D. Evaluations of cellular lattice structures manufactured using selective laser melting. *International Journal of Machine Tools and Manufacture* **62**, 32–38 (2012).

[10] Sairajan KK, Aglietti GS, Mani KM. A review of multifunctional structure technology for aerospace applications. Acta Astronaut 2016; 120:30–42.

[11] Fleck NA, Deshpande VS, Ashby MF. Micro-architectured materials: past, present and future. Proc R Soc A 2010; 466:2495–516.

[12] Cutolo, A., Engelen, B., Desmet, W. & Van Hooreweder, B. Mechanical properties of

diamond lattice Ti–6Al–4V structures produced by laser powder bed fusion: On the effect of the load direction. *Journal of the Mechanical Behavior of Biomedical Materials* **104**, 103656 (2020).

[13] Ngo TD, Kashani A, Imbalzano G, Nguyen KTQ, Hui D (2018) Additive manufacturing (3D printing): A review of materials, methods, applications and challenges. Compos Part B Eng 143: 172–196.

[14] Kelly, C. N. *et al.* Fatigue behavior of As-built selective laser melted titanium scaffolds with sheet-based gyroid microarchitecture for bone tissue engineering. *Acta Biomaterialia* **94**, 610–626 (2019).

[15] Chouhan, G., Gunji, B. M., Bidare, P., Ramakrishna, D. & Kumar, R. Experimental and numerical investigation of 3D printed bio-inspired lattice structures for mechanical behaviour under Quasi static loading conditions. *Materials Today Communications* 35, 105658 (2023).

[16] Kothandaraman, L. & Balasubramanian, N. K. Optimization of FDM printing parameters for square lattice structures: Improving mechanical characteristics. *Materials Today: Proceedings* (2024).

[17] Sokolsky-Papkov, M., Agashi, K., Olaye, A., Shakesheff, K. & Domb, A. J. Polymer carriers for drug delivery in tissue engineering. *Advanced Drug Delivery Reviews* **59**, 187–206 (2007).

[18] Del Guercio, G., Galati, M. & Saboori, A. Electron beam melting of Ti-6Al-4V lattice structures: correlation between post heat treatment and mechanical properties. Int J Adv Manuf Technol 116, 3535–3547 (2021).

[19] Ngo TD, Kashani A, Imbalzano G, Nguyen KTQ, Hui D (2018) Additive manufacturing (3D printing): A review of materials, methods, applications and challenges. Compos Part B Eng

143: 172–196.

[20] Chouhan, G., Gunji, B. M., Bidare, P., Ramakrishna, D. & Kumar, R. Experimental and numerical investigation of 3D printed bio-inspired lattice structures for mechanical behaviour under Quasi static loading conditions. *Materials Today Communications* 35, 105658 (2023).

[21] Arakawa, C. K. & DeForest, C. A. Polymer Design and Development. in *Biology and Engineering of Stem Cell Niches* 295–314 (Elsevier, 2017).

[22] Chen, S. Y. *et al.* Microstructure and fracture properties of open-cell porous Ti-6Al-4V with high porosity fabricated by electron beam melting. *Materials Characterization* **138**, 255–262 (2018).

[23] Chen, Z. *et al.* Influence of the pore size and porosity of selective laser melted Ti6Al4V ELI porous scaffold on cell proliferation, osteogenesis and bone ingrowth. *Materials Science and Engineering: C* **106**, 110289 (2020).

[24] Zhou, H. *et al.* Lightweight structure of a phase-change thermal controller based on lattice cells manufactured by SLM. *Chinese Journal of Aeronautics* **32**, 1727–1732 (2019).

CHAPTER II

Introduction to Additive Manufacturing

2.1 Definition

Additive manufacturing is a relatively new manufacturing process that has sparked widespread attention in a variety of industries. Additive manufacturing, also known as 3D printing, is the technique of creating a physical product from a three-dimensional digital model. It fabricates an object by applying consecutive thin layers of a material, such as plastic, metal, resin, or even biomaterials-based on a computerized design developed with computer-aided design (CAD) software [1,2]. The method starts with slicing the digital 3D model into multiple thin layers. The 3D printer then follows these instructions, carefully depositing material layer by layer to gradually produce the physical thing.

2.2 Historical evolution

2.2.1. Origins and early developments (1980-1990)

Hideo Kodama first described the 3D printing method in 1981 at the Municipal Industrial Research Institute in Nagoya, Japan [3,4]. He invented two additive methods for fabricating 3D plastic models, by photo-hardening photopolymer using UV light. Hideo Kodama's success launched the scramble to patent 3D printing technology.

In 1984, French General Electric Company researchers filed a patent application for their stereolithographic technology [5]. The patent application was unsuccessful due to the method's perceived lack of commercial potential.

Also in 1984, American researcher Chuck Hull of 3D Systems Corporation successfully submitted his own patent for a stereolithography fabrication technique [6]. Finally, he developed a feasible production process for 3D printing. Hull's contributions to current 3D printing include the STL file format, digital slicing, and infill. Chuck Hull is now considered as the inventor of 3D printing [7,8].

Scott Crump devised fused deposition modeling (FDM), a consumer-oriented 3D printing technology, in 1989 [9]. FDM involved extruding plastic to create three-dimensional objects. The 1980s were a pivotal time of invention for the additive manufacturing movement. From here, we can plot the progression of 3D printing on a timeline.

2.2.2 Evolution of 3D printing technologies (1990-2000)

EOS GmbH, which had only been founded a year before, produced the EOS system in 1990, the first commercial 3D printer designed for industrial applications. EOS stereos are still regarded as excellent, albeit obsolete, devices. By 1992, Stratasys had built on Scott Crump's work and filed their own patent for FDM 3D printing [10]. The FDM patent was a significant milestone since it enabled the development of residential 3D printers.

Solidscape revolutionized the game in 1993 with its dot-on-dot 3D printing process [8]. This technology incorporated polymer-jet manufacturing for high-accuracy models. Other players used MIT's inkjet print head technology to create commercially viable 3D printers.

During the mid-1990s, novel material deposition techniques emerged from Stanford and Carnegie Mellon University, notably microcasting [11] and sprayed materials [12]. Subsequently, sacrificial and support materials gained prominence, thereby facilitating the realization of innovative object geometries [13].

In 1995, the Fraunhofer Institute offered Selective Laser Melting (SLM) to the public. In the same year, Z Corporation formed a relationship with MIT to develop new 3D printing technologies, including commercial FDM.

3D printing had its first push into healthcare. In 1999, scientists at the Wake Forest Institute for Regenerative Medicine employed it to create a synthetic scaffold to support organs grown from human cells. This was an important milestone since it demonstrated the wonders of 3D printing and its potential applications in other industries.

2.2.3. Expansion and diversification (2000-2010)

When the term "additive manufacturing" was coined in 2000, 3D printing evolved from a buzzword into a movement. Over the last decade, 3D printers have spread from the commercial space to our homes.

The wonderful folks at Object Geometries created the first inkjet 3D printer, and Z Corporation created the first successful multi-color 3D printer. The following year marked a watershed moment in 3D printing.

In 2001, the first desktop 3D printer was introduced by Solidimension. The first desktop 3D printer was a huge success. In 2002, the Wake Forest Institute for Regenerative Medicine used biomedical 3D printing to create a 3D-printed tiny kidney with the same characteristics as a human kidney [8].

The RepRap Project was founded in 2005 with the goal of making open-source DIY 3D printers available to everyone. The project was a success when the RepRap Darwin became the first 3D printer capable of creating its own parts. RepRap is where the term Fused Filament Fabrication (FFF) originated, replacing the term FDM.

Similarly, Evan Malone and Hod Lipson launched the Fab@Home project in 2006 with the goal of designing a low-cost and open-source manufacturing system that users could develop on their own and provide comments on, making the project very collaborative [14].

Between 2005 and 2008, the 3D printing community concentrated on producing prostheses and human aid items for public use. Much of the 3D printing software available to the public at the time was open source, which allowed it to be swiftly distributed and modified by a large number of individual users. The first functional prosthetic leg was 3D printed in 2008. 3D printing for healthcare progressed, with Organovo creating the first 3D-printed blood vessel in 2009. The patents covering the Fused Deposition Modeling (FDM) printing technique expired in 2009. This paved the way for a new wave of startup companies, many of which were founded by key contributors to these open-source initiatives, with the purpose of making commercial FDM 3D printers more accessible to the public [15].

2.2.4. Domestication and safety concerns (2010-2019)

While techniques like casting, fabrication, stamping, and machining are still more prevalent in metalworking compared to AM, additive manufacturing is gaining ground. With the advantages of designing for AM, engineers can anticipate even greater progress in the future. Additionally, 3D printing has facilitated the incorporation of various features that enhance accuracy, precision, ease of use, and innovative capabilities. AM is making huge advances in the aviation industry. The

11

aviation industry always desires fuel-efficient [16] and convenient jet engines [17]. AM is carefully considered to reduce costs, reduce the number of nonconforming parts, reduce engine weight to increase fuel efficiency and discover new, highly complex shapes that would be impossible to manufacture using traditional methods.

As technology advanced, numerous authors speculated that 3D printing could help with sustainable development in developing countries [18]. Urbee made history in engineering when it created the first 3D-printed automobile in 2011. The first 3D-printable pistol was introduced in 2012, generating severe security worries regarding home 3D printing. In 2014, the first 3D-printed house was constructed in China, demonstrating the relevance of 3D printing in building and construction.

In 2014, Benjamin S. Cook and Manos M. Tentzeris revealed the first multi-material, vertically integrated printed electronics additive manufacturing platform (VIPRE), allowing for 3D printing of functional electronics functioning at up to 40 GHz [19].

New filament types were developed, and the ability to 3D print them improved. Naturally, NASA tried 3D printing food and apparel in 2014 and 2015. In 2016, the first human bones were created [8], reigniting interest in 3D printing for regenerative purposes. In 2017, new software was developed to improve mass production using 3D printers, prompting firms from numerous industries to establish 3D printing farms [20].

2.2.5. Looking to the future (2020-present)

3D printers have achieved a level of quality and affordability that permits many people to participate in the 3D printing revolution. 3D bioprinting is receiving significant attention in the medical field due to its numerous potential applications. This technology offers various advantages,

such as creating human tissue for burn victims and fabricating human organs for transplants. In November 2021, Steve Verze, a British patient, received the world's first totally 3D-printed prosthetic eye at Moorfields Eye Hospital in London [21].

3D printing for architecture is advancing and is expected to grow significantly in the coming years. The University of Maine unveiled the Factory of the Future 1.0, the world's largest 3D printer, in April 2024. It can create things up to 29 meters [22].

In 2024, researchers employed machine learning to improve the fabrication of synthetic bone [23] and established a new shock absorption record [24]. The potential of 3D printing is far from being fully realized, with numerous projects and remarkable stories yet to emerge.

2.3 General principles (how does 3D printing work?)

3D printing is a novel production and processing technology. Ordinary printers use ink to print artwork and text on 2D paper, but 3D printers use heat, light, laser, and other methods to convert raw materials (such as metals, ceramics, and polymers) into thin layers. The layers are then joined together to form an object in space. Unlike traditional techniques, 3D printing has fewer steps, allowing you to print more easily. In general, four phases are involved in printing a model using 3D printing: 3D modeling, data preparation, printing process, and finishing (or post-processing), as shown in Fig. 2.1.
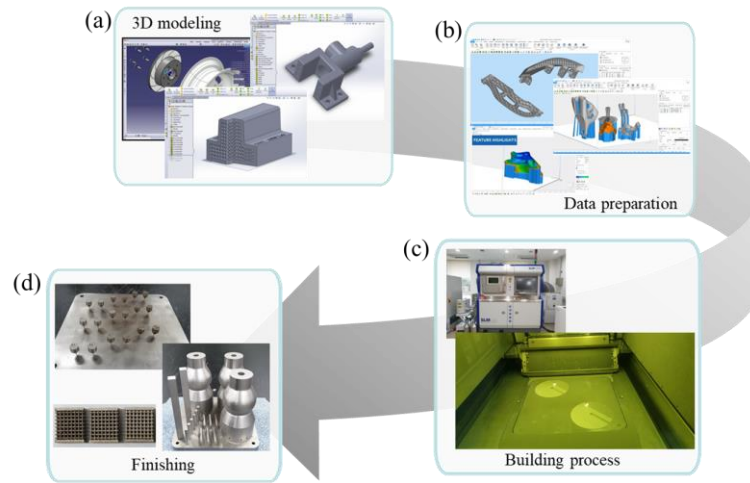
Figure 2.1. 3D printing process sequence, (a) 3D modeling, (b) data preparation, (c) building process, (d) finishing.

2.3.1. 3D modeling

3D printable models can be made using a computer-aided design (CAD) package, a 3D scanner, or a standard digital camera and photogrammetry software. 3D printed models generated with CAD produce fewer errors than conventional approaches. Errors in 3D printable models can be detected and addressed before printing. 3D scanning is the process of gathering digital data about the shape and appearance of a physical thing and constructing a digital model from it.

CAD models can be saved in stereolithography file format (STL), which is a de facto CAD file format for additive manufacturing that holds data based on CAD model surface triangulations. STL is unsuitable for additive manufacturing because it produces enormous file sizes of topology-optimized parts and lattice structures due to the large number of surfaces involved [25]. To address this issue, a redesigned CAD file format known as additive manufacturing file format (AMF) was established in 2011. It saves data via curved triangulations [26].

2.3.2. Data preparation

The model in STL format should consist of closed, connected triangles without any overlapping, ensuring that each edge is part of two triangles. Errors often occur during the conversion of CAD files to STL, which could affect the 3D printing process. Prior to 3D printing from an STL file, it's important to check for defects (errors). Most CAD software generates errors in output STL files of the following types:

- Holes or gaps in a mesh
- Flipped normals
- Intersecting and overlapping triangles
- Bad edges
- Noise shells

A stage in the STL production known as "repair" corrects such issues in the original model [27]. STLs produced from a model obtained through 3D scanning typically include more of these errors [28], as 3D scanning is frequently accomplished using point-to-point acquisition/mapping. 3D reconstruction frequently contains inaccuracies [29].

Support systems are also set up to ensure 3D printing construction capabilities. These support systems must be easily removed and must support overhang structures and allow heat transfer.

Once completed, the STL file must be processed by software known as a "slicer". This software turns the model into a series of thin layers and generates a "code file" with instructions specific to a certain type of 3D printer and printing parameter process [30]. The "code file" can then be printed using 3D printing client software.

2.3.3. Building process (printing)

The AM contains multiple sorts of processes that differ in the raw materials utilized, the source of energy used to form and bind material during deposition, and the way the material is deposited to make an artifact. Each method has unique manufacturing features and capabilities, allowing for a variety of design options.

Printer resolution describes layer thickness (Z direction) and X-Y resolution in dots per inch (dpi) or micrometers (μm). Layer thickness and X-Y resolution depend on each 3D printing method, which has different build speeds, accuracies, and print sizes. For example, the layer thickness in the SLM process ranges from 30 to 100 μm. The X-Y resolution depends mainly on the power source (e.g. laser diameter). Higher resolution settings result in larger files with no enhancement in print quality.

Constructing a model with contemporary methods can take several hours to several days, depending on the method, size, and complexity of the number of models produced simultaneously.

2.3.4. Finishing (post-processing)

Though printer-produced resolution and surface quality are enough for some applications, post-processing and finishing procedures provide advantages such as increased dimensional accuracy, smoother surfaces.

Sanding and bead blasting are examples of subtractive processes that can improve the surface polish of a 3D-printed component. When smoothing pieces that require dimensional accuracy, it is critical to consider the amount of the material being removed [31].

Some printed polymers, such as acrylonitrile butadiene styrene (ABS), can have their surface finish smoothed and improved utilizing chemical vapor methods [32] that use acetone or comparable solvents.

Annealing can be useful as a post-processing step for several additive manufacturing processes. Annealing a 3D-printed item improves internal layer bonding by recrystallizing the part. It provides for an improvement in mechanical qualities, including fracture toughness, flexural strength, impact resistance, and heat resistance [33]. Annealing a component may not be appropriate for applications requiring dimensional accuracy since it might cause warpage or shrinkage owing to heating and cooling [34].

The layered nature of classic additive manufacturing technologies causes a stair-stepping effect on part surfaces that are curved or inclined in relation to the construction platform. The effect is highly dependent on the layer height utilized, as well as the orientation of a portion of the surface throughout the construction process [35].

Additive or subtractive hybrid manufacturing (ASHM) is a process that involves creating a 3D-printed component and then removing material by machining [36]. Depending on the application, machining operations can be conducted after each layer or after the full 3D print. These hybrid approaches enable 3D-printed items to attain superior surface qualities and dimensional precision [37].

2.4 Additive Manufacturing Processes

There are seven primary types of 3D printing technologies in use today (Fig. 2.2), with over 20 variants. The primary distinctions between methods are in how layers are deposited to form pieces

and the materials employed. Each process has advantages and disadvantages, which is why some companies provide an option between powder and polymer for the material used to construct the product. The major factors to consider when selecting a machine are normally speed, the cost of the 3D printer and produced prototype, material selection and pricing.
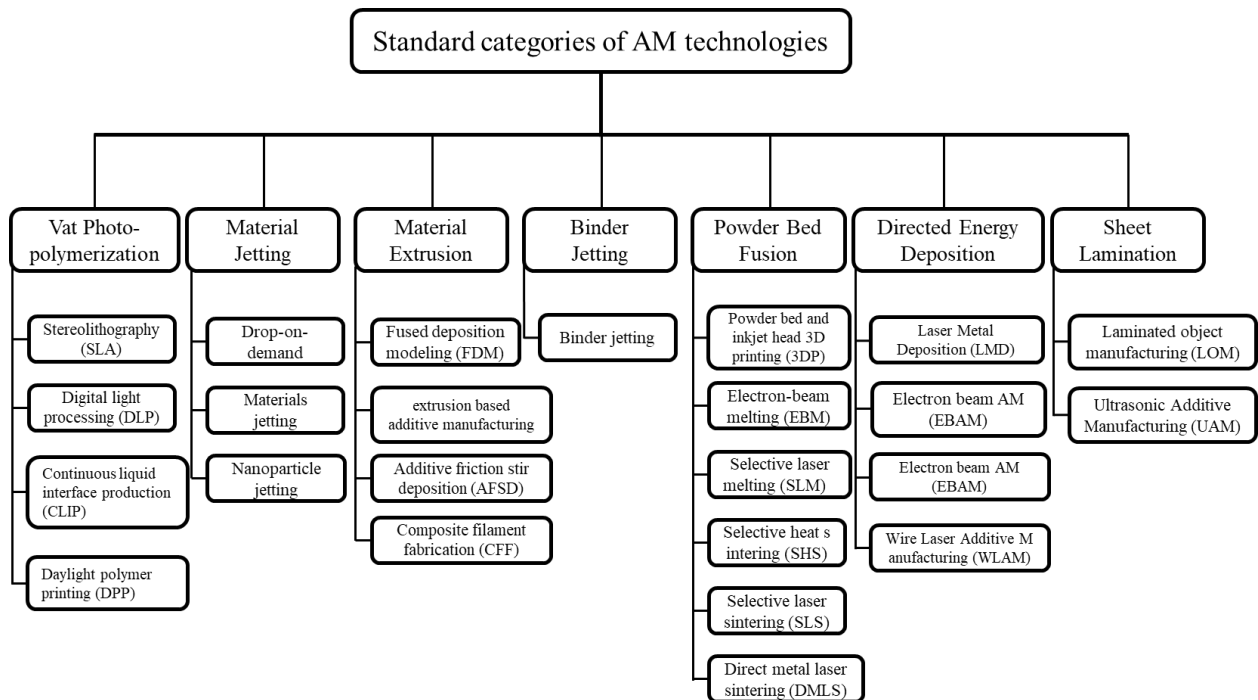
Figure 2.2. Seven AM processes and types of AM technologies in the category [38].

2.4.1. Vat Photopolymerization

Vat photopolymerization is an additive manufacturing technology that produces solid objects using photopolymer resins that solidify when exposed to light. Figure 2.3 shows the three primary configurations. The scanning SLA and TPP are presented in top-down arrangements, whilst the

MPSL is shown in bottom-up settings. Vector scanning SLA involves scanning a fine laser beam over the resin surface with scanning galvanometers [39].

In these 3D printers, a vat retains the liquid resin, while a construction platform is immersed near the surface. A CAD file guides a light source to cure the resin layer by layer. The platform is then re-submerged to continue the process until the object is completely produced. As the process involves the use of liquid to form objects, the material does not offer structural support during the building phase, as it utilizes unbound material.
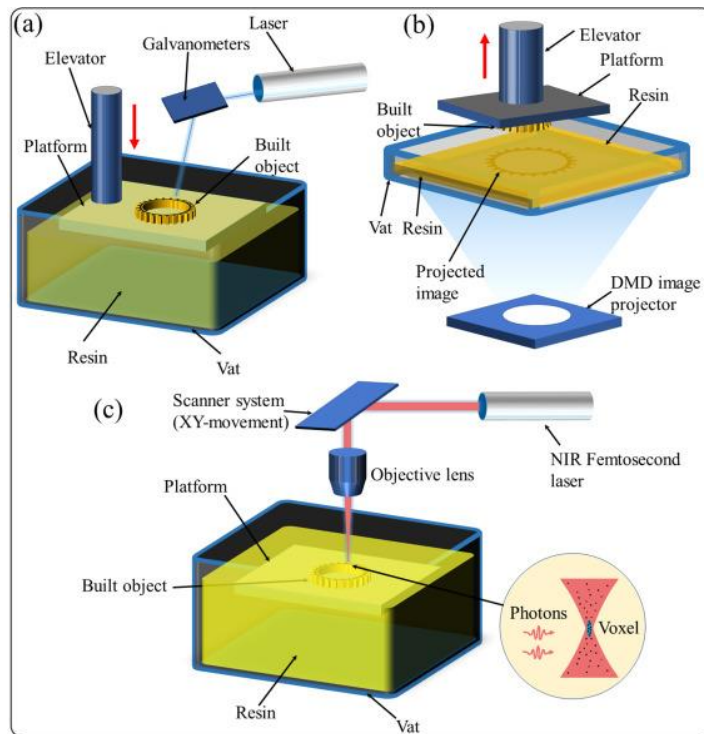
Figure 2.3. (a) Scheme of bottom-up mask projection stereolithography (MPSL). (b) Scheme of the traditional laser-based stereolithography (SLA). (c) Scheme of two-photon polymerization (TPP) (Reprinted from [39] with permission).

This process is noted for its speed and accuracy, which allows for large-scale model printing. However, photopolymers lack robust structural properties, which can lead to deterioration and deformation over time. Furthermore, parts may require specific handling or specialized tooling, making the process more expensive in particular applications. The most popular vat photopolymerization 3D printing technologies include the following:

- Stereolithography (SLA): Also known as SL, optical fabrication, photo-solidification, or resin printing, SLA uses a concentrated beam of ultraviolet light or a laser to focus onto the surface of a vat filled with liquid photopolymer. This process creates each layer of the desired 3D object by cross-linking or degrading a polymer.

- Digital light processing (DLP): In the DLP process, a digital projector screen flashes a single image of each layer across the entire platform simultaneously. Each layer image is composed of square pixels, forming small rectangular bricks called voxels. DLP can achieve faster print times for some parts since each layer is exposed all at once rather than being drawn out with a laser.

- Continuous liquid interface production (CLIP): CLIP uses a tank of resin with a transparent section at the bottom called the window. An ultraviolet light beam shines through the window, illuminating the precise cross-section of the object, causing the resin to solidify (photopolymerize). The object rises slowly, allowing the resin to flow under and maintain contact with the bottom of the object. An oxygen-permeable membrane creates a dead zone, preventing the resin from attaching to the window and enabling continuous photopolymerization. This process is significantly faster than traditional SLA, claiming speeds up to 100 times faster than other commercial 3D printing methods.

- Daylight polymer printing (DPP) utilizes an LCD (Liquid Crystal Display) instead of a laser or projector to cure the polymer. Also known as LCD 3D printing, this technique uses unmodified LCD screens and a specially formulated daylight polymer.

2.4.2. Material jetting

Material jetting produces items in a similar way to a two-dimensional inkjet printer, uses photopolymers, metals, or wax that harden under light or heat [40]. This approach creates items layer by layer and allows multiple materials to be printed on the same part.

Material jetting dispenses photopolymer through a printer equipped with hundreds of small nozzles, quickly creating parts layer by layer. UV radiation cures and solidifies each layer. Support structures made of dissolvable material must be printed at the same time and removed during post-processing.

Material jetting encompasses several processes, the most popular of which are:

- Drop-on-demand (DOD) printers use two jets: one for building materials and one for dissolvable support. They follow a preset path, depositing material pointwise to create a component layer by layer. A fly cutter ensures that the surface is flat before adding each subsequent layer. DOD is commonly used to create wax patterns for lost wax casting and mold production, making it an indirect 3D printing method.

- Materials jetting (MJ) sprays ultra-thin layers of photopolymer onto a build tray in a manner similar to inkjet printing. Each layer is quickly cured with UV light, resulting in fully finished models that are ready for use. The gel-like support substance, which is ideal for complex designs, is simply removed by hand or with water jetting.

- Nanoparticle jetting (NPJ) employs a liquid incorporating nanoparticles of construction or support material. The liquid is jetted onto the build tray in thin layers, and high temperatures force it to evaporate, leaving just the solid substance. This technique is suited for both metals and ceramics.

Material jetting 3D printing is perfect for producing realistic prototypes with fine detail, precision, and smooth surfaces. It enables the printing of several colors and materials in a single print, eliminating the need for separate STL files for each material or color. To combine colors or properties, export the design as an OBJ or VRML file that supports texture and full-color designations. However, this method is expensive, and UV-activated photopolymers used in material jetting can degrade mechanical characteristics and become brittle over time.

The number of materials that can be used is limited because they must be deposited in drops. Polymers and waxes are ideal and widely utilized materials because of their viscous nature and ability to create drops.

2.4.3. Binder jetting

The binder jetting 3D printing technique involves the deposition of a binding adhesive compound onto layers of material, which are commonly powdered. The materials can be ceramic or metal. This approach is sometimes referred to as an inkjet 3D printing system. To create the item, the printer uses a head that moves over the platform base and deposits, one layer at a time, by spreading a layer of powder (plaster or resin) and printing a binder in the cross-section of the part using an inkjet-like technique (Fig 2.4). This process is repeated until all layers have been printed. This method enables the printing of full-color prototypes, overhangs, and elastomer parts.

Impregnation using wax or thermoset polymer increases the robustness of bound powder prints [41].
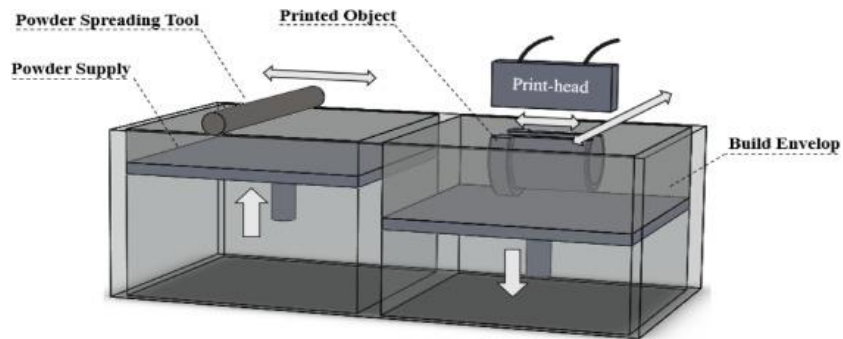
Figure 2.4. Schematic representation of the binder jetting (Reprinted from [41] with permission).

Binder jetting 3D printing is compatible with a wide range of materials, including metals, sands, and ceramics. Some materials, such as sand, may not require additional processing. Binder jetting is ideal for applications requiring high aesthetics and shape, including architectural models, packaging, toys, and figurines. However, the fragile nature of the pieces makes them unsuitable for functional purposes.

The infiltration procedure allows metal-based binder jetting objects to have rather good mechanical characteristics. As a result of the infiltration process, they can be functioning components with generally good mechanical qualities. The binder jetting approach has the advantage of not using heat during the construction process, which prevents the formation of residual stresses in the pieces. They are also less expensive than SLM (Selective Laser Melting) or DMLS (Direct Metal Laser Sintering) metal parts, but their mechanical qualities are inferior since the grains of the materials do not completely fuse together.

There are several varieties of 3D printing binder materials, each designed for a unique application. They are classified as furan binder (for sand casting applications), phenolic binder (for sand molds and cores), silicate binder (for ecologically friendly sand molds and cores), and aqueous-based binder (for metals).

2.4.4. Powder Bed Fusion (PBF)

Powder Bed Fusion (PBF) is a 3D printing technique that combines powdered material point by point with an energy source, usually a laser or electron beam (Fig. 2.5). It is a popular approach for industrial additive manufacturing (AM) and may be used with both metals and polymers; however, not all materials are suitable.

A recoater blade or roller applies a thin layer of powder to a building surface. The energy source selectively melts or sinters the material required for that layer. The construction plate then falls to make place for the next layer, and the procedure is repeated.

Variables affecting PBF include laser or beam power, spot size, hatch design, layer height, and powder quality. Historically, establishing these methods required extensive trial and error, particularly with metals. However, advances in artificial intelligence, machine learning, simulation, and sensors are making PBF more predictable and easier to apply.
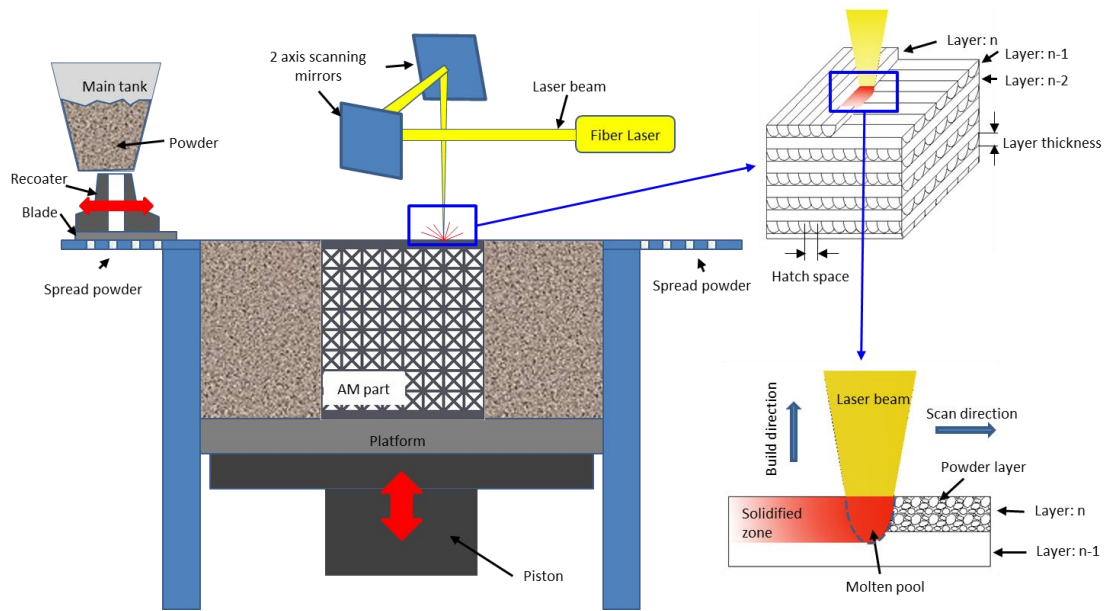
Figure 2.5. Schematic representation of SLM.

Here are a few of the most notable of PBF:

- Selective Laser Sintering (SLS) is a 3D printing technology for polymer powders, most commonly thermoplastics, but thermosets are becoming available. The powdered material is dispersed across the bed and selectively melted using a laser. The construction plate is then lowered, and the process continues. The surrounding powder supports the components during printing, removing the need for extra support structures. Unused powder can frequently be sieved and reused, sometimes in combination with new material.

- Selective laser melting (SLM) is similar to SLS but is used with metals. A recoater blade or roller applies powdered metal to a substrate, and a laser melts the powder for each layer. Unlike SLS, pieces are fused to the substrate and frequently require support structures to stabilise overhangs and aid with heat control, however better technology

울산대학교
UNIVERSITY OF ULSAN

and software can reduce or remove the requirement for these supports. Because metal powders are flammable, SLM is carried out in an inert atmosphere, such as argon, or under vacuum conditions. Unused powder can be reused, but it may deteriorate over time due to oxidization.

- Electron Beam Melting (EBM) is a powder bed fusion technique for metals. An EBM printer works similarly to a small-scale particle accelerator, blasting electrons at the powder bed under a vacuum to melt the metal material rather than utilizing a laser. To keep particles from dispersing owing to charge, each layer of material is often pre-sintered before the printing process begins, and the entire print bed is kept heated during the build. Parts are printed inside a semi-sintered cake of powder, which strengthens the structure and often removes the need for extra support structures. However, some EBM versions allow parts to be sintered in loose powder.

2.4.5. Material extrusion

Material extrusion is the process of 3D printing employing a continuous strand of thermoplastic material. The filament is fed from a coil into a heated printer extruder head (extruder). The molten material is pushed out of the extruder's nozzle and placed on a heated 3D printing substrate to improve adhesion. After the first layer is finished, the extruder advances to deposit following layers directly onto the developing workpiece. The extruder head is computer controlled and normally moves along at least three dimensions in Cartesian systems, but polar and delta systems are also popular. This process continues layer by layer until the thing is completely constructed.

This technology, known as fused filament fabrication (FFF), is popular among hobbyists for 3D printing. Stratasys commercialized it under the name fused deposition modeling (FDM), a

concept coined by S. Scott Crump in the late 1980s [9]. Following the expiration of the FDM patent, a substantial open-source community known as RepRap arose, along with several commercial and DIY implementations of the technology. This has resulted in much lower expenses. However, material extrusion has limited dimensional precision and produces highly anisotropic products.

The most frequent materials used in material extrusion are thermoplastics such as acrylonitrile butadiene styrene (ABS), aliphatic polyamides (PA or Nylon), high-impact polystyrene (HIPS), polylactic acid (PLA), and thermoplastic polyurethane (TPU). This technology has recently been utilized successfully to extrude sophisticated plastic materials like polyether ether ketone (PEEK) and polyetherimide (PEI), as well as paste-like materials, including ceramics, concrete, and chocolate [42].

Material extrusion can also be used with composite materials, provided the base thermoplastic is present in sufficient quantities to achieve layer fusion. This permits printed goods to include elements such as wood, metal, and carbon fiber.

2.4.6. Directed Energy Deposition (DED)

Directed Energy Deposition (DED) produces parts by melting and depositing material onto a workpiece layer by layer. This additive manufacturing process is crucial when working with metal powders or wire source materials (Fig. 2.6). Other names for DED include laser-engineered net shaping, directed light fabrication, direct metal deposition, Laser Deposition Welding (LDW), and 3D laser cladding. DED can repair complex broken parts like turbine blades or propellers in addition to manufacturing new ones from scratch, which is frequently done with a hybrid CNC mill/turn tool.

DED 3D printers are typically huge industrial devices that require a closed, regulated environment. They include a nozzle positioned on a multi-axis arm inside a closed frame that deposits melted material onto the workpiece surface, where it solidifies. The method is similar to material extrusion, but the DED nozzle can move in several directions, frequently with up to 5-axes or 6-axes systems [43].
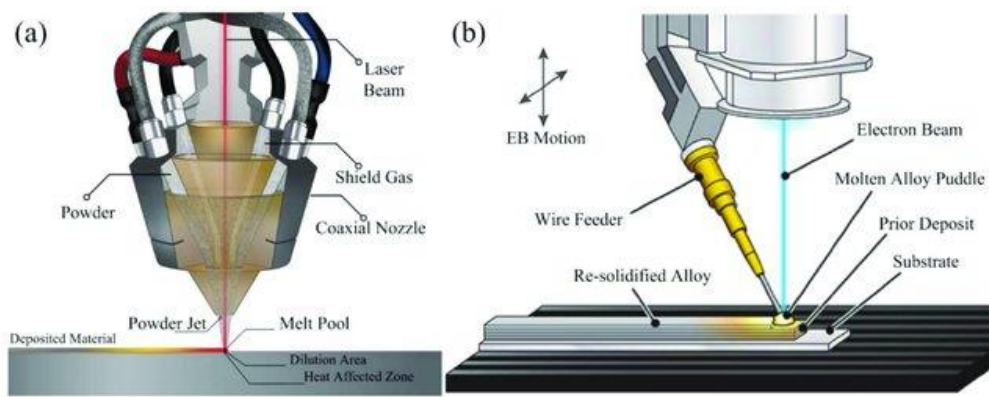
Figure 2.6. Directed Energy Deposition (DED): (a) Powder DED (laser source), (b) Wire DED (E-beam source) [44].

DED refers to several various technologies, each with a focus on how materials are fused and customized to specific applications [45]. The many DED procedures prominently include:

- Powder DED systems, including laser metal deposition (LMD) and laser engineered net shaping (LENS), utilize a nozzle to disperse powder onto the part's surface. A laser beam then melts the powder, creating material layers ranging from 0.1 mm to a few millimeters in thickness. This process, known as a "blown powder" AM method, offers high precision and involves the automated deposition of material layers. One of its key characteristics is the metallurgical bonding of the cladding material with the base

material, as well as the absence of undercutting, setting it apart from other welding techniques due to its low heat input into the substrate.

- Wire DED systems, like wire laser metal deposition (WLMD), introduce wire through a nozzle where it is melted by a laser. This process employs inert gas shielding in either an open environment (with gas surrounding the laser) or in a sealed gas enclosure or chamber. Wire DED delivers superior deposition rates in comparison to both powder bed and blown powder DED methods.

- Electron Beam Additive Manufacturing (EBAM): EBAM creates large-scale metal structures by melting wire feedstock using an electron beam. It can attain high deposition rates and works with metals like titanium, and nickel, allowing for both manufacturing and repair of industrial components.

- Laser Deposition Welding (LDW) and Hybrid Manufacturing: LDW combines a powder nozzle for metal deposition with a 5-axis milling machine. This hybrid approach combines the versatility of additive manufacturing with the precision of traditional machining, allowing for the creation of high-quality metal parts.

These DED technologies can 3D print a wide range of metals, including aluminum, copper, titanium, stainless steel, and several steel alloys. Each approach has its own set of constraints and material compatibilities, making it appropriate for a wide range of industrial applications, including aerospace and consumer electronics.

2.4.7. Sheet lamination (SL)

Sheet Lamination (SL) is the method of creating a three-dimensional object by stacking and laminating thin sheets of material. The lamination method can be bonding, ultrasonic welding, or brazing, with laser cutting or CNC machining providing the final shape [45]. SL technologies include techniques such as Ultrasonic Additive Manufacturing (UAM) and Laminated Object Manufacturing (LOM).

LOM uses layers of paper connected with adhesive in a cross-hatching pattern to allow for easy removal after printing. LOM is generally used for aesthetic and visual modeling, not structural applications. Its low cost and short manufacturing time enable product designers to create low-fidelity prototypes using readily available low-cost materials. A schematic overview of the original LOM is shown in Fig. 2.6.
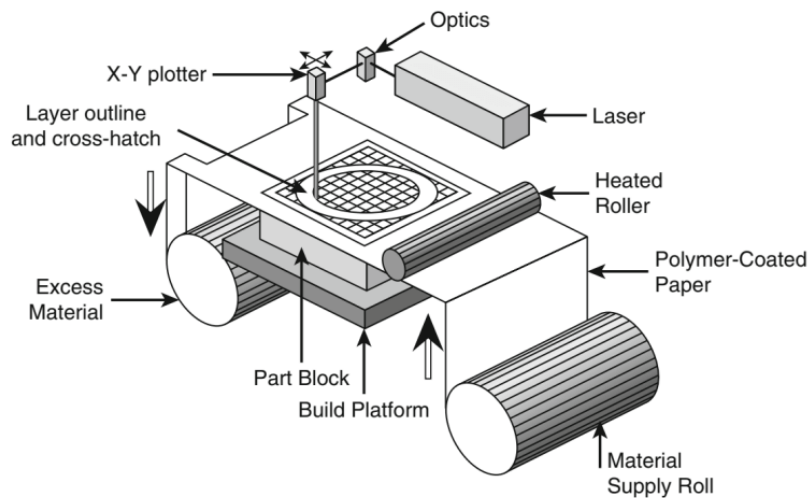
Figure 2.7. Schematics of sheet lamination (Reprinted from [45] with permission).

UAM uses metal sheets or ribbons bonded together using ultrasonic welding. This approach frequently employs CNC machining to eliminate loose metal during the welding process. UAM works with metals including aluminum, copper, stainless steel, and titanium. It operates at low temperatures, allowing to produce complex interior structures without melting the metal. The procedure enables for bonding diverse materials and utilizes relatively less energy compared to processes that involve melting metals.

2.5 Application of AM in metal forming (forming dies)

Manufacturing dies (or molds) entails a distinctive array of challenges, encompassing the processing of tough alloys, the attainment of micron-level precision, the fabrication of intricate part geometries, and the fulfillment of mounting requirements for expedited production at reduced expenses [46]. Traditional tooling methods involving processes like machining and casting are time-consuming, costly, and limiting for complex or high-precision tools and low-volume or rapidly changing high-volume products [6]. In contrast, AM technologies enable cost-effective and fast tool production, reduce material waste, and provide design freedom. AM technologies allow for greater customization and design freedom, overcoming the limitations of conventional tools. The global tooling industry faces challenges in molding and hot stamping processes due to cooling times and high costs for low-volume production [48-50]. However, to address these challenges, Additive Manufacturing (AM) technologies offer promising opportunities for tool making. This section provides an overview of AM processes in tooling applications and discusses the application of AM technologies in the molding and metal-forming industries.

2.5.1. AM materials

The selection of tool material exerts a substantial influence on tool lifespan, which is contingent upon the performance demands of the intended application and the tool manufacturing process. Performance factors like toughness, wear resistance, hot hardness, and resistance to softening assume critical roles in ensuring optimal tool performance throughout its operational lifespan [46].

In the realm of cold working tools such as stamping tools and dies, potential failure mechanisms encompass abrasive wear, adhesive wear, mixed wear from sliding contact, fatigue-induced chipping at edges, localized plastic deformation exceeding yield strength, fatigue, and galling. The selection of tool concepts (material, hardness, surface roughness, and treatment) is intrinsically connected to the characteristics of the workpiece material, including grade, surface condition, and thickness.

Conversely, in the hot-working tools used in high-pressure die casting, hot forging, hot stamping, or extrusion, potential failure modes comprise thermal fatigue (heat checking), corrosion/erosion, total failure from cracking, and indentation. These tools must possess properties such as low thermal expansion coefficient, high thermal conductivity, high hot yield strength, resistance to softening at high temperatures, high creep strength, and ductility to withstand deformation, softening, wear, impact loading, and corrosion/erosion at elevated working temperatures. An overview of L-PBF powder materials from various suppliers demonstrates substantial variations in mechanical properties (Table 2.1).

Table 2.1. Mechanical properties of AMed materials of hot work tool steels [50].

Materials	Tensile strength (MPa)	Hardness (HRC)	Thermal conductivity (W/mK)
1.2709	2040	-	-
H11	1505	56	-
H13	1990	50	22.7
1.2367	1457	55	27
CR7V-L	1600	56	24.5
HTCS-130	1314	50	50.8

2.5.2. Topology optimization

Metal additive manufacturing (AM) allows for the flexible production of tools, reducing lead time and minimizing economic impacts [51,52]. The production cost for metal AM tools is considerably higher than that of conventional methods. However, the cost of AM tools can be reduced through topology optimization [53]. Topology optimization enables the design of parts with freeform geometry to be optimized for specific objectives such as weight, strength, or stiffness. By reducing overall tool material while maintaining strength, the build time on the AM system can be decreased, resulting in lower tool costs.

Laser Powder Bed Fusion (L-PBF) was used to manufacture cylinder punches 100mm long with a piercing diameter of 10mm using materials H13, M300, and KP4. These punches were tested on 1.2 mm thick CP1180 sheet steel with a tensile strength of 1200 MPa. The M300 punch had the best mechanical qualities among the AM punches, outperforming the traditional SKD11 and HWS punches with 10,000 strokes [54].

While AM has the potential to reduce material waste and enable rapid prototyping, the high cost of metal powders and AM equipment is a significant consideration. Balancing these costs with the benefits of improved die performance and reduced lead times is crucial to assess the potential for widespread adoption. Leal *et al.* [2] created stamping inserts using L-PBF in maraging steel 1.2709 to investigate the use of additive manufacturing for automotive stamping. After heat treatment and machining, the AM stamping inserts reached a final hardness of 57 HRC and withstood one million strokes. Although this method increased the costs by more than double, it reduced the lead time by half compared to conventional toolmaking.

Asnafi *et al.* [53] investigated topology optimization of stamping tools, including U-bending and punch manufactured using the L-PBF process. The results revealed that the topology-optimized U-bending tool showcased a 19.4% reduction in weight and an 11.1% decrease in lead time compared to the solid tool (Fig. 2.8). Moreover, in contrast to a solid punch, implementing a honeycomb inner structure and volume fraction optimization led to material usage and printing time reductions of approximately 45% and 34%, respectively (Fig. 2.9).
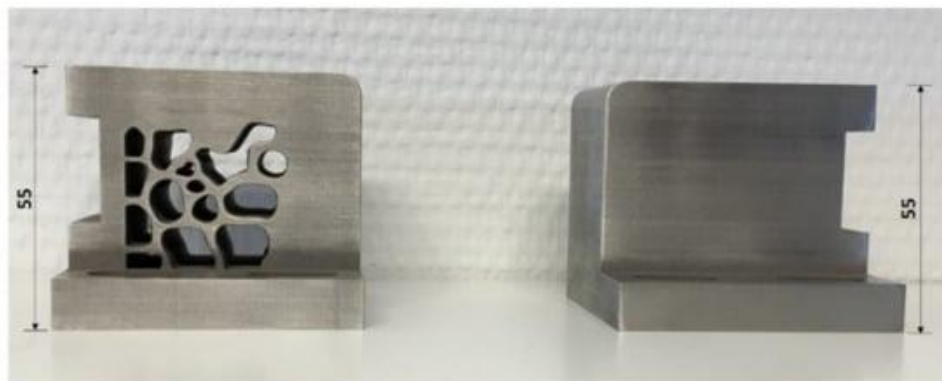
Figure 2.8. The U-bending tool: (a) topology optimized at the volume fraction of 0.45, (b) 3D-printed as a solid piece. (Reprinted from [53] with permission).
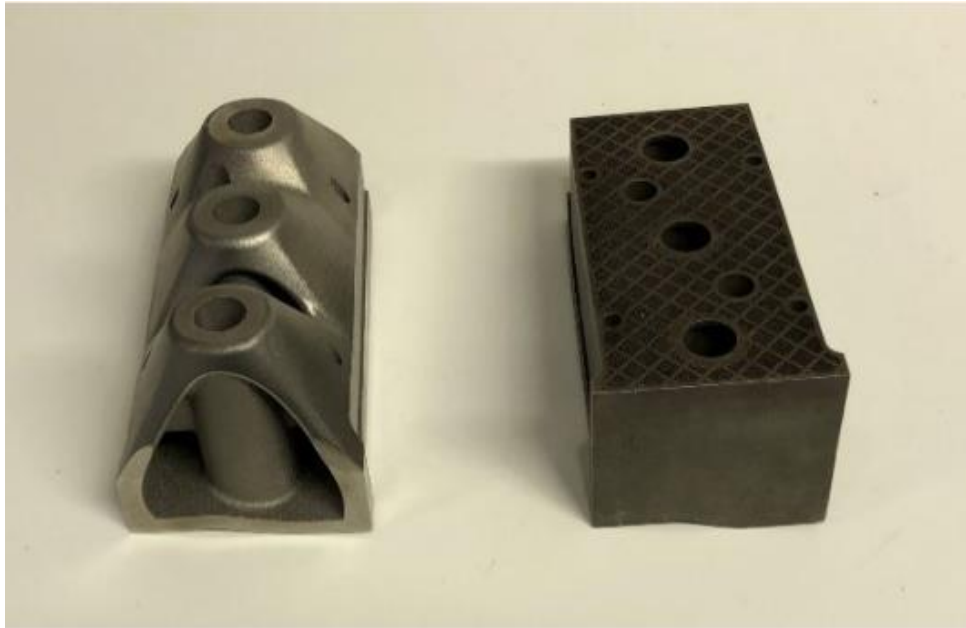
Figure 2.9. Two versions of the 3D-printed industrial punch, (a) topology optimization using LS-TaSC, (b) with a honeycomb inner structure. (Reprinted from [53] with permission).

Alimov et al. [4] designed hot-forming dies that were tailored for additive manufacturing, specifically using wire arc direct energy deposition (WA-DED) and L-PBF technologies. These dies were designed with a lightweight 2D-lattice structure, resulting in a 56% reduction in die weight. Maraging steel 17-4PH was chosen for its high processability despite slightly lower mechanical properties. Industrial forging tests confirmed that the manufactured dies were indeed workable.

2.5.3. Conformal cooling channels

Hot working in metallurgy refers to processes in which metals are plastically deformed above their recrystallization temperature, allowing them to recrystallize during deformation. This prevents strain hardening, maintaining low yield strength and hardness while keeping ductility high [55]. Hot working includes various processes such as rolling, forging, extrusion, and drawing, and contrasts with cold working, which is performed below the recrystallization temperature.

Hot stamping is a well-known technology for producing structural parts from advanced steel and aluminum alloys [56,57]. One of the primary benefits of hot forming is the ability to make high-strength components while using low-forming loads, hence reducing springback. However, the technique requires high temperatures for material formation and precision cooling to achieve desired component qualities, demanding advanced tooling designs. The design of press tools often incorporates internal cooling channels and utilizes conventional machining processes, such as drilling and casting, to achieve the desired cooling rate. One significant challenge associated with current cooling channel manufacturing methods is the inability to form channels with an equidistant profile from the tool surface, resulting in inconsistent cooling rates throughout the part [58].

Conformal cooling (CC) channels are a series of cooling channels positioned uniformly near mold cavity surfaces. They offer significant advantages over conventional straight-drilled cooling systems by providing more uniform and efficient cooling, thereby improving production quality and efficiency [50]. Key design characteristics such as channel shape, size, and position are critical for attaining uniform and quick cooling while accounting for cooling performance, mechanical strength, and coolant pressure drop. AM enables the creation of conformal cooling channels within

the die, which follow the shape of the part being formed. This improves heat dissipation and reduces cycle times, leading to higher production efficiency and better part quality.

Lin and Chou [60] employed an analytical model founded on the energy balance principle and specific cycle times to compute the average temperature of the tool surface. Through these computations, they derived the diameter of the cooling channels and stipulated a suggested range of cooling diameters for various blank thicknesses, as outlined in Table 2.2.

Table 2.2 Cooling channel diameter guideline based on blank thickness [60].

Blank thickness, t (mm)	Cooling channel diameter, d (mm)
t≤2	8≤d≤10
2≤t≤4	10≤d≤12
4≤t≤6	12≤d≤14

Cortina *et al.* [61] investigated the design of efficient cooling channels, which were built using AM on a CR7V-L hot-worked steel basis before being milled for post-processing. The cooling channels were made from filler materials such as AISI H13 and AISI 316L laser cladding (see Fig. 2.10). Their findings showed that the thermal performance of additively and conventionally built cooling channels was substantially comparable.
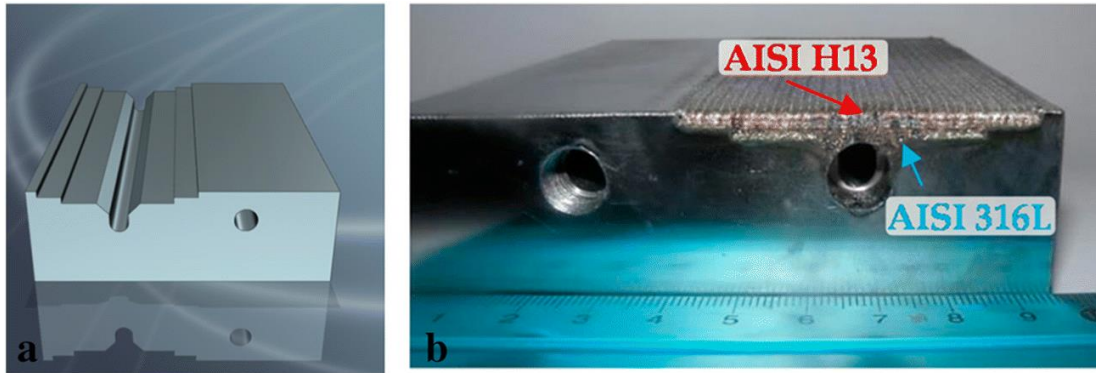
Figure 2.10. (a) Initial CR7V-L substrate with one drilled channel and prepared machined surfaces for cladding, (b) Finished sample with one drilled and one additively manufactured cooling channel (Reprinted from [61] with permission).

AM enables the creation of conformal cooling channels within the die, which follow the shape of the part being formed. This improves heat dissipation and reduces cycle times, leading to higher production efficiency and better part quality. Müller *et al.* [62] found that using additive manufacturing to fabricate complex cooling channels following the profile of the parts significantly reduced quenching time during hot stamping processes. The cooling system was redesigned through simulations, and the key input parameters were the compression force, workpiece temperature, coolant temperature, flow rate, and internal surface roughness of the cooling channels. The AMed cooling system revealed significant improvements in both temperature gradient and temperature on the die's operative surface (see Fig. 2.11).
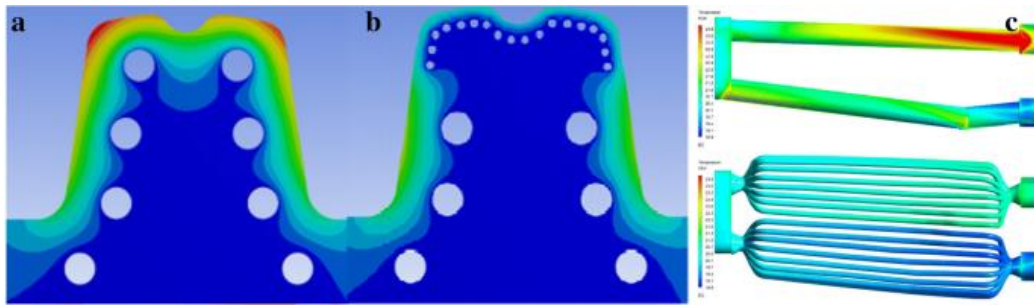
Figure 2.11. (a) Conventional drilled cooling channels (max temperature in the tool 191 °C), (b) optimized cooling channels (max temperature 81 °C), (c) comparison of the temperature gradient in the conventional and optimized cooling system (Reprinted from [62] with permission).

Wang *et al.* [63] presented an automated methodology for creating efficient cooling circuits, a critical factor in enhancing product quality and productivity during rapid machining. These tailored cooling channels are designed to conform to the product's shape closely, minimize cooling time, and achieve uniform temperature distribution to control volumetric shrinkage (Fig. 2.12). The simulation results provided empirical evidence of the efficacy of the cooling circuit generated through this algorithm.
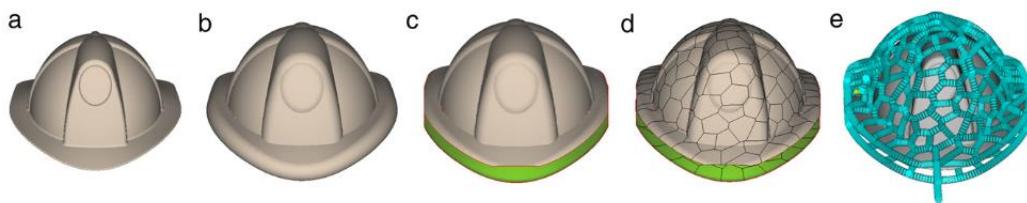
Figure 2.12. Overview of the cooling circuit generation algorithm: (a) a given model to be fabricated by rapid tooling, (b) the offset surface of the given model, (c) the separated offset surface serving as the conformal surface, (d) the refined discrete CVD, and (e) the resulting conformal cooling circuit [63].

The flexibility of AM allows for the creation of innovative and sustainable hot stamping tools with improved quenching capabilities compared to traditional methods. Researchers have investigated the application of lattice structures in hot stamping dies to harness the design flexibility offered by additive manufacturing (AM). These lattice structures are utilized to insulate specific sections of the die near cooling channels, thereby decreasing thermal mass and enhancing cooling efficiency. Tan *et al.* [64] designed an innovative injection mold with large self-supporting cooling channels and a suitable porous structure to improve cooling efficiency and reduce production costs. Chantzis *et al.* [50] suggested incorporating lattice structures into hot stamping tools to decrease thermal mass and enhance heat absorption and cooling rates (Fig. 2.13). Through a 2D thermo-mechanical finite element analysis model and Design of Experiments (DoE), the optimized design achieves a balance between cooling performance and structural integrity. The results demonstrated that lattice structures improve cooling efficiency and reduce AM build time by requiring less material. Brooks & Brigden [65] introduced the concept of conformal cooling layers, which enhance heat transfer rates and reduce temperature variation in tooling (Fig. 2.14). These cooling layers are filled with self-supporting, repeatable unit cells forming a lattice that increases fluid vorticity and improves convective heat transfer. Mechanical testing revealed that the design of these unit cells has a considerable impact on compression performance (Fig. 2.15).
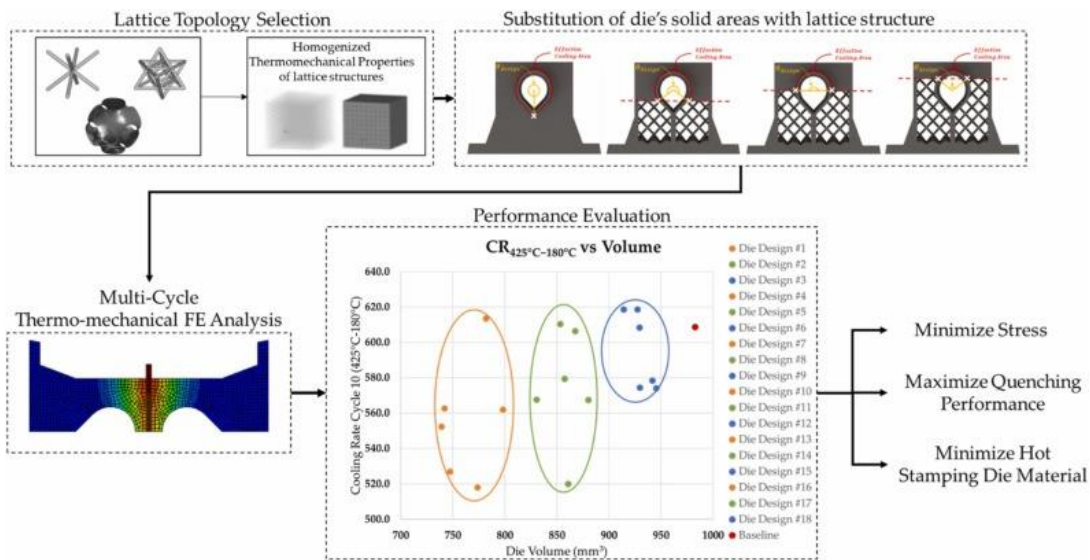
Figure 2.13. Overview of the proposed design optimisation workflow. (Reprinted from [64] with permission).
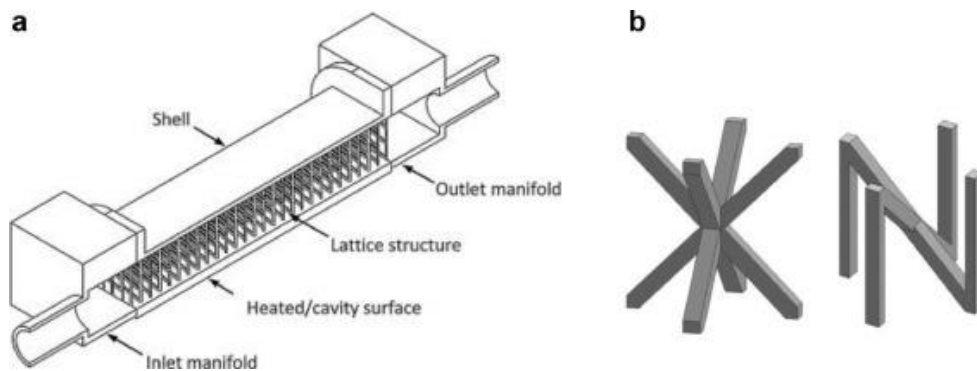
Figure 2.14. CC layer and its unit cells proposed by Brooks and Brigden: (a) overview of the CC layer and (b) unit cells: cross (left) and N (right) (Reprinted from [65] with permission).

41
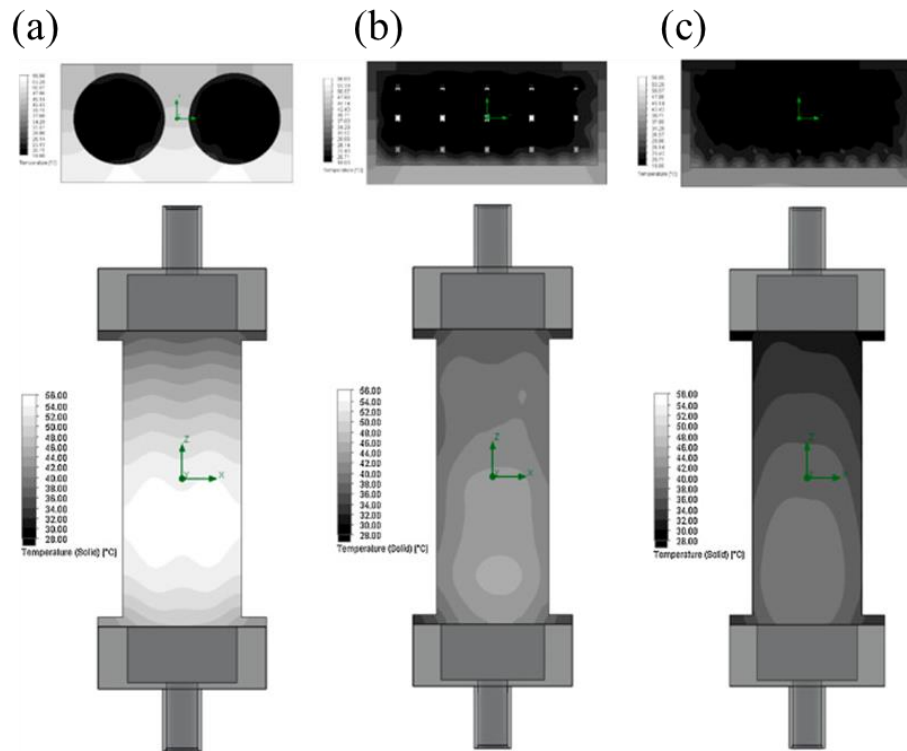
Figure 2.15. FEA mid-plane and bottom surface temperature plots of the three test pieces, (a) drilled holes, (b) cross lattice, (c) N lattice (Reprinted from [65] with permission).

2.5.4 Conclusions

The advancement of AM has facilitated the creation of cost-effective, fast, and highly efficient tooling for metal forming. A range of AM technologies is now accessible to accommodate both low and high-volume production, tailored to specific application requirements. Through thoughtful material selection, tool design, and simulation processes, AM tooling can effectively rival traditional machining techniques to fulfill the metal forming needs of many industries.

References

[1] Gao, W. et al. The status, challenges, and future of additive manufacturing in engineering. Computer-Aided Design 69, 65–89 (2015).

[2] Ngo, T. D., Kashani, A., Imbalzano, G., Nguyen, K. T. Q. & Hui, D. Additive manufacturing (3D printing): A review of materials, methods, applications and challenges. Composites Part B: Engineering 143, 172–196 (2018).

[3] Hideo, K. A Scheme for Three-Dimensional Display by Automatic Fabrication of Three-Dimensional Model, IEICE Transactions on Electronics (Japanese Edition), vol. J64-C, No. 4, pp. 237–41, April 1981.

[4] Hideo, K. Automatic method for fabricating a three-dimensional plastic model with photo-hardening polymer, Review of Scientific Instruments, Vol. 52, No. 11, pp. 1770–73, November 1981.

[5] Jean-Claude, Andre. Disdpositif pour realiser un modele de piece industrielle. National De La Propriete Industrielle. Archived from the original on 5 February 2016. Retrieved 5 February 2016.

[6] 3D Printing: What You Need to Know. PCMag.com. Archived from the original on 18 October 2013. Retrieved 30 October 2013.

[7] Apparatus for Production of Three-Dimensional Objects by Stereolithography (8 August 1984).

[8] History of 3D Printing: When Was 3D Printing Invented? All3DP. 10 December 2018. Archived from the original on 3 July 2019. Retrieved 22 November 2019.

[9] U.S. patent 5,121,329, June 9, 1989. Apparatus and Method for Creating Three-Dimensional Objects. (A system and a method for building three-dimensional objects in a layer-by-layer manner via fused deposition modeling).

[10] U.S. patent 5,340,433, August 23, 1994. Modeling Apparatus for Three-Dimensional Objects (An apparatus for building three-dimensional objects via fused deposition modeling).

[11] Amon, C. H., Beuth, J. L., Weiss, L. E., Merz, R. & Prinz, F. B. Shape Deposition Manufacturing With Microcasting: Processing, Thermal and Mechanical Issues. Journal of Manufacturing Science and Engineering 120, 656–665 (1998).

[12] Weiss, L. E. Manufacturing Mechatronics Using Thermal Spray Shape Deposition. Preprint at https://doi.org/10.15781/T23N20X5T (2018).

[13] Prinz, F. B.; Merz, R.; Weiss, Lee. Ikawa, N. (ed.). Building Parts You Could Not Build Before. Proceedings of the 8th International Conference on Production Engineering. London, UK: Chapman & Hall. pp. 40–44 (1997).

[14] Malone, E. & Lipson, H. Fab@Home: the personal desktop fabricator kit. Rapid Prototyping Journal 13, 245–255 (2007).

[15] Matias, E. & Rao, B. 3D printing: On its historical evolution and the implications for business. in 2015 Portland International Conference on Management of Engineering and Technology (PICMET) 551–558 (IEEE, Portland, OR, USA, 2015).

[16] Han, P. Additive Design and Manufacturing of Jet Engine Parts. Engineering 3, 648–652 (2017).

[17] Scott, C. GE Aviation Tests the Largest Jet Engine in the World, Featuring 3D Printed Fuel Nozzles. 3D Print (2016).

[18] R.Ishengoma, F. & B. Mtaho, A. 3D Printing: Developing Countries Perspectives. IJCA 104, 30–34 (2014).

[19] Cook, Benjamin Stassen. Vertical integration of inkjet-printed RF circuits and systems (VIPRE) for wireless sensing and inter/intra-chip communication applications (2014).

[20] Hai Alami, A. et al. 3D printing in the food industry: Recent progress and role in achieving sustainable development goals. Ain Shams Engineering Journal 15, 102386 (2024).

[21] Patient receives the world's first fully 3D-printed prosthetic eye. Engadget.com. (2021).

[22] World's biggest 3D printer whirs into action. www.bbc.com (2024).

[23] University of Illinois at Urbana-Champaign (25 May 2024). Synthetic Bones Designed by AI Set to Transform Orthopedic Surgery. SciTechDaily. (2024).

[24] Salas, J. Autonomous robot invents the world's best shock absorber. New Atlas (2024).

[25] New ASTM Additive Manufacturing Specification Answers Need for Standard Interchange File Format ASTM, July 20, 2011.

[26] F42 Committee. Specification for Additive Manufacturing File Format (AMF) Version 1.2. doi:10.1520/F2915-20.

[27] Magic, the Most Powerful 3D Printing Software | Software for Additive Manufacturing. Software.materialise.com (2016).

[28] How to repair a 3D scan for printing. Anamarva.com (2016).

[29] Bernardini, F. & Rushmeier, H. The 3D Model Acquisition Pipeline. Computer Graphics Forum 21, 149–172 (2002).

[30] Satyanarayana, B. & Prakash, K. J. Component Replication Using 3D Printing Technology. Procedia Materials Science 10, 263–269 (2015).

[31] How to Smooth 3D-Printed Parts. Machine Design (2014).

[32] Kraft, Caleb. Smoothing Out Your 3D Prints With Acetone Vapor. Make (2014).

[33] Benwood, C., Anstey, A., Andrzejewski, J., Misra, M. & Mohanty, A. K. Improving the Impact Strength and Heat Resistance of 3D Printed Models: Structure, Property, and Processing Correlationships during Fused Deposition Modeling (FDM) of Poly(Lactic Acid).

ACS Omega 3, 4400–4411 (2018).

[34] Wijnbergen, D. C., Van Der Stelt, M. & Verhamme, L. M. The effect of annealing on deformation and mechanical strength of tough PLA and its application in 3D printed prosthetic sockets. RPJ 27, 81–89 (2021).

[35] Delfs, P., Ťows, M. & Schmid, H.-J. Optimized build orientation of additive manufactured parts for improved surface quality and build time. Additive Manufacturing 12, 314–320 (2016).

[36] Du, W., Bai, Q. & Zhang, B. A Novel Method for Additive/Subtractive Hybrid Manufacturing of Metallic Parts. Procedia Manufacturing 5, 1018–1030 (2016).

[37] Li, F., Chen, S., Shi, J. & Tian, H. Investigation on Surface Quality in a Hybrid Manufacturing System Combining Wire and Arc Additive Manufacturing and Machining. in Transactions on Intelligent Welding Manufacturing (eds. Chen, S., Zhang, Y. & Feng, Z.) 127–137 (Springer Singapore, Singapore, 2018).

[38] Adugna, Y. W., Akessa, A. D. & Lemu, H. G. Overview study on challenges of additive manufacturing for a healthcare application. IOP Conf. Ser.: Mater. Sci. Eng. 1201, 012041 (2021).

[39] Zhang, F. et al. The recent development of vat photopolymerization: A review. Additive Manufacturing 48, 102423 (2021).

[40] Elkaseer, A. et al. Material jetting for advanced applications: A state-of-the-art review, gaps and future directions. Additive Manufacturing 60, 103270 (2022).

[41] Ziaee, M. & Crane, N. B. Binder jetting: A review of process, materials, and methods. Additive Manufacturing 28, 781–801 (2019).

[42] Zhuo, P., Li, S., Ashcroft, I. A. & Jones, A. I. Material extrusion additive manufacturing of

continuous fibre reinforced polymer matrix composites: A review and outlook. Composites Part B: Engineering 224, 109143 (2021).

[43] Li, L., Haghighi, A. & Yang, Y. A novel 6-axis hybrid additive-subtractive manufacturing process: Design and case studies. Journal of Manufacturing Processes 33, 150–160 (2018).

[44] Selema, A., Ibrahim, M. N. & Sergeant, P. Metal Additive Manufacturing for Electrical Machines: Technology Review and Latest Advancements. Energies 15, 1076 (2022).

[45] Gibson, I., Rosen, D. & Stucker, B. Additive Manufacturing Technologies: 3D Printing, Rapid Prototyping, and Direct Digital Manufacturing. (Springer New York, New York, NY, 2015). doi:10.1007/978-1-4939-2113-3.

[46] Altan, T., Lilly, B., Yen, Y. C. & Altan, T. Manufacturing of Dies and Molds. CIRP Annals 50, 404–422 (2001).

[47] S.N.A. Shahbudin, M.H. Othman, S.Y.M. Amin, M.H.I. Ibrahim, A review of metal injection molding- Process, optimization, defects and microwave sintering on WC-Co cemented carbide IOP Conf. Ser. Mater. Sci. Eng., 226 (2017), Article 012162.

[48] E. Sachs, E. Wylonis, S. Allen, M. Cima, H. Guo (2000) Production of Injection Molding Tooling With Conformal Cooling Channels Using the Three Dimensional Printing Process, Polymer Eng. And Sci, Vol. 40.

[49] M. Mazur, P. Brincat, M. Leary, M. Brandt (2017) Numerical and experimental evaluation of a conformally cooled H13 steel injection mould manufactured with selective laser melting. Int. J. Adv. Manuf. Technol., 93, pp. 881–900.

[50] Chantzis, D. et al. Review on additive manufacturing of tooling for hot stamping. Int J Adv Manuf Technol 109, 87–107 (2020).

[51] Garrett, B. 3D Printing: New Economic Paradigms and Strategic Shifts. Global Policy 5, 70–

75 (2014).

[52] Weller, C., Kleer, R. & Piller, F. T. Economic implications of 3D printing: Market structure models in light of additive manufacturing revisited. International Journal of Production Economics 164, 43–56 (2015).

[53] Asnafi, N., Rajalampi, J. & Aspenberg, D. Design and Validation of 3D-Printed Tools for Stamping of DP600. IOP Conf. Ser.: Mater. Sci. Eng. 651, 012010 (2019).

[54] Li, R. et al. Additive manufacturing (AM) of piercing punches by the PBF method of metal 3D printing using mold steel powder materials. J Mech Sci Technol 33, 809–817 (2019).

[55] Saby, M., Bouchard, P.-O. & Bernacki, M. Void closure criteria for hot metal forming: A review. Journal of Manufacturing Processes 19, 239–250 (2015).

[56] Ismail, A., Mohamed, M. S. Review on sheet metal forming process of aluminium alloys. 17th International Conference on Applied Mechanics and Mechanical Engineering. pp. 19–21 (2016).

[57] Taylor, T., Clough, A. Critical review of automotive hot-stamped sheet steel from an industrial perspective. Mater Sci Technol 34:809–861 (2018).

[58] S.A. Jahan, T. Wu, Y. Zhang, H. El-Mounayri, A. Tovar, J. Zhang, D. Acheson, R. Nalim, X. Guo, W.H. Lee (2016) Implementation of conformal cooling & topology optimization in 3D printed stainless steel porous structure injection molds, Procedia Manuf. 5, 901–915.

[59] Park, H. S., & Dang, X. P. Design and simulation-based optimization of cooling channels for plastic injection mold. New Technologies-Trends, Innovations and Research, 2, 19-44 (2012).

[60] Lin, Z.-C. & Chou, M.-H. Design of the cooling channels in nonrectangular plastic flat injection mold. Journal of Manufacturing Systems 21, 167–186 (2002).

[61] Cortina, M., Arrizubieta, J., Calleja, A., Ukar, E. & Alberdi, A. Case Study to Illustrate the

Potential of Conformal Cooling Channels for Hot Stamping Dies Manufactured Using Hybrid Process of Laser Metal Deposition (LMD) and Milling. Metals 8, 102 (2018).

[62] Müller, B., Gebauer, M., Hund, R., Malek, R., & Gerth, N. Metal Additive Manufacturing for tooling applications-Laser Beam Melting technology increases efficiency of dies and molds. In Metal Additive Manufacturing Conference MAMC (2014).

[63] Wang, Y., Yu, K.-M., Wang, C. C. L. & Zhang, Y. Automatic design of conformal cooling circuits for rapid tooling. Computer-Aided Design 43, 1001–1010 (2011).

[64] Tan, C. et al. Design and additive manufacturing of novel conformal cooling molds. Materials & Design 196, 109147 (2020).

[65] Brooks, H. & Brigden, K. Design of conformal cooling layers with self-supporting lattices for additively manufactured tooling. Additive Manufacturing 11, 16–22 (2016).

CHAPTER III

Mechanical Analysis of SUS316L, Tool Steel, Ti, and AlSi10Mg Lattice Structures Manufactured by Laser-Powder Bed Fusion for Energy Absorption Design

3.1 Introduction

Additive manufacturing (AM) technology presents significant advantages, including efficient material utilization [1], seamless process integration [2], and enhanced mechanical properties [3,4]. From an engineering design standpoint, AM techniques such as powder bed fusion (PBF) and directed energy deposition (DED) offer heightened flexibility, vastly improving manufacturing capabilities beyond those possible with traditional methods [5-7]. Laser powder bed fusion (L-PBF), a laser-based AM process, enables the fabrication of highly precise and intricate shapes with a normal resolution of approximately 100 micrometers [8-10]. This design freedom facilitates the realization of lightweight lattice structures essential in the mobility industry, with active exploration of applications in both design and manufacturing processes [11,12]. These lattice structures have the potential to optimize product design, reduce manufacturing time, and minimize material usage in AM by minimizing component volume [11].

Lattice structures are recognized for their exceptional mechanical properties, high energy absorption capacity, and lightweight, rendering them valuable in diverse industries such as aerospace, automotive, and biomedical devices [13-18]. Traditional manufacturing methods for lattice structures, such as melt foaming [19], powder metallurgy [20], brazing [21], or casting [22], are known for their high costs and potential shape and density inaccuracies. Previous research on lattice structures has predominantly focused on their mechanical properties, including Young's

modulus, collapse stress, deformation behavior, and energy absorption capacity, utilizing experimental, theoretical, and numerical approaches [23-28]. For instance, Yan et al. [29] investigated the strength and compressive modulus of gyroid cellular lattice structures with varying unit cell sizes, while Li et al. [30] examined the effects of layer and cell numbers on the compressive responses of body-centered cubic with vertical struts (BCCZ) aluminum lattice structures through compression tests and finite element analysis (FEA). Their findings indicated a notable decrease in modulus and strength with increasing layer number.

Various studies have been conducted to investigate lattice design and its impact on mechanical behaviors. Previous research has focused on popular 3D strut-based architectures such as the face-centered cubic (FCC), body-centered cubic (BCC), and their variations [31]. Additionally, Xiao et al. [32] assessed the mechanical properties of three stainless steel lattice structures (FCC, vertex cubic (VC), and edge-centered cubic (ECC)) based on optimization results. Furthermore, Smith et al. [33] proposed the addition of struts to original cell architectures in the loading direction (BCCZ, face-centered cubic with vertical struts (FCCZ)) to enhance their mechanical performance. It is anticipated that BCCXYZ and FCCXYZ, featuring struts in three loading directions, will exhibit increased load capacity and isotropic cell topology.

A variety of materials have been utilized in fabricating lattice structures using the L-PBF method. Titanium alloys and stainless steels are extensively employed in medical applications due to their high biocompatibility, corrosion resistance, and suitable mechanical properties [34,35]. Additionally, aluminum alloys are frequently chosen for their inherent properties such as lightweight, high specific strength, and good thermal conductivity [23-25,36]. Furthermore, due to their superior strength, tool steels have been utilized in injection molds or hot stamping dies with complex cooling systems [37-38]. Nevertheless, previous studies on AMed lattice structures

51

were predominantly conducted using a single material, making it challenging to ascertain the influence of the base material on the mechanical performances of lattice structures prepared by the L-PBF method.

This study aims to experimentally investigate and compare the compressive mechanical behavior of AMed FCCXYZ lattice structures with different base materials. Quasi-static compression tests were carried out to analyze the deformation behavior and mechanical properties of the structures under compressive loads. Subsequently, Gibson-Ashby models were formulated based on the experimental results. Furthermore, the energy absorption capabilities of the lattice structures were evaluated and analyzed.

3.2 Experimental set-up

3.2.1. Sample design

In this research, we utilized commercial software (Solidworks, Dassault Systèmes, Vélizy-Villacoublay, France) to create samples incorporating the FCCXYZ lattice unit cell, depicted in Fig. 3.1a. The unit cell was comprised of cylindrical struts measuring 2.5 mm in length. The strut diameters ranged from 0.3 mm to 0.6 mm in increments of 0.05 mm. Configurations for compression tests were designed by amalgamating 8×8×8-unit cells with lower and upper skin sheets, each possessing a 1.5 mm thickness, as illustrated in Fig. 3.1b. To quantify the lightweight properties of the AMed samples, we defined the relative density (RD) as the ratio of cellular density (ρ^*) to bulk material density (ρ_s). The RD (ρ^*/ρ_s) of the FCCXYZ lattice structure with cylindrical struts of diameter d and length l can be presented for low RD as:

$$\frac{\rho^*}{\rho_s} = \frac{\rho_{lattice}}{\rho_{solid}} = \frac{3\pi}{4}\left(1 + 2\sqrt{2}\right)\left(\frac{d}{l}\right)^2 \tag{1}$$

In the context of high relative density (RD), it is crucial to account for the joint volume when determining the RD. Gibson [14] proposed an equation for vertex-corrected RD as follows:

$$\frac{\rho^*}{\rho_s} = \frac{3\pi}{4}\left(1 + 2\sqrt{2}\right)\left(\frac{d}{l}\right)^2 - C\left(\frac{d}{l}\right)^3 \tag{2}$$

Given that the RD values under consideration in this study span a range from low to high, it was imperative for the sake of consistency to calculate all RDs using Eqn. (2). The RD values calculated in the course of this work fell within the range of 0.11 to 0.36. For the geometric data, a *C* value of 11.50 was utilized with the Solidworks software.

(a) 2.5 mm
Strut diameters: 0.3 - 0.6 mm

(b) 23 mm, 20 mm, 20 mm
8×8×8 unit cells
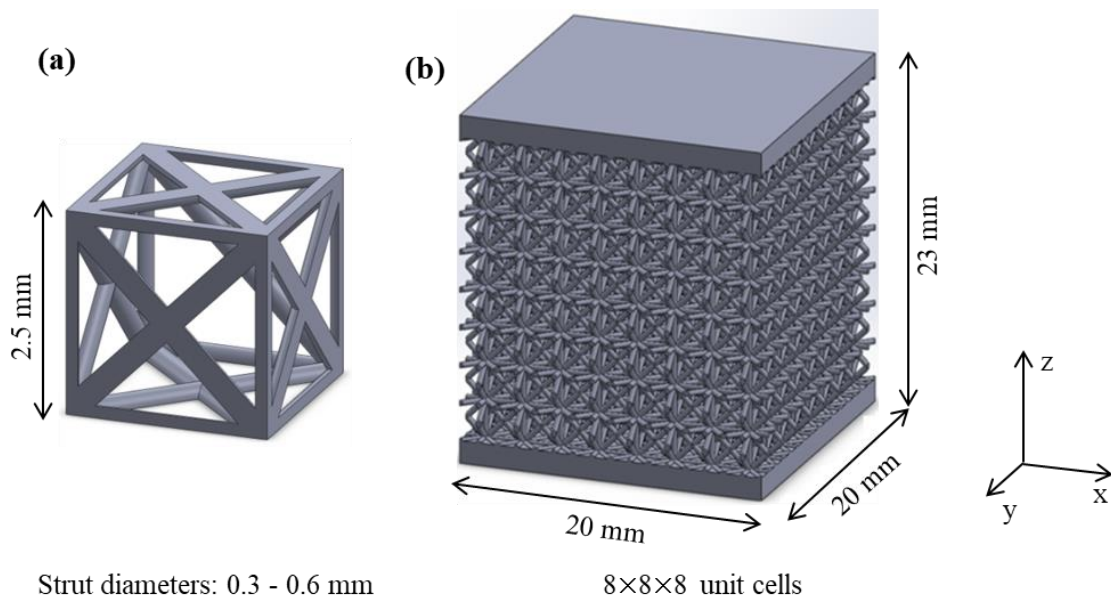
Figure 3.1. Schematics of (a) FCCXYZ unit cell and its dimensions, (b) FCCXYZ lattice structure design for compression testing.

3.2.2. Equipment, materials, and printing conditions

The manufacturing process utilized selective laser melting (SLM) 3D printers (SLM 280 series, SLM Solutions GmbH, Lübeck, Germany). These printers were equipped with single and twin laser sources, each with a 400 W capacity. The build chamber was purged with argon gas, and precise process parameters were established to fabricate both solid and lattice structure samples with exceptional precision and bulk density ($> 99.6\%$), as outlined in Table 3.1. When processing SUS316L and tool steel 1.2709 powders (particle size: $10 - 45$ µm), the specimens were fabricated on a platform heated to 100 °C, with a layer thickness of 30 µm. In contrast, for AlTi10Mg and Ti-Gr.2 powders (particle size: $20 - 63$ µm), the platform temperature was elevated to 200 °C. The chemical compositions of the metal powders and detailed process parameters can be found in Tables 3.1 and 3.2, respectively.

Table 3.1. L-PBF process parameters

Material	Laser power (W)	Hatch distance (µm)	Speed (mm/s)	Layer thickness (µm)	3D printing machine
SUS316L	190	120	750	30	SLM 280 HL
Tool steel1.2709	220	120	800	30	SLM 280 HL
Ti-Gr.2	350	120	1400	30	SLM 280
AlSi10Mg	350	190	900	30	SLM 280

Table 3.2. Chemical composition of metal powders (provided by SLM Solutions GmbH)

Material	Elements (wt%) (maximum)											
	Fe	Ti	Al	C	Co	Mn	Mo	Cr	Ni	Si	N	O
SUS316L	Bal.	-	-	0.03	-	0.2	3.0	28.0	14.0	1.0	0.1	
Tool steel 1.2709	Bal.	0.8	0.15	0.03	9.5	0.1	5.2	-	19	0.1	0.1	0.04
Ti-Gr.2	0.3	Bal.	-	0.08	9.5	-	-	-	-	-	0.03	0.25
AlSi10Mg	0.55	-	Bal.	0.05	-	0.45	-	-	0.05	11.0	-	-

In the Laser Powder Bed Fusion (L-PBF) type additive manufacturing (AM) process, the orientation of target objects plays a critical role in influencing residual stress, overhang structure, and build time. The modification of the original design for the AM process was carried out using the Magics software (Materialise NV, Leuven, Belgium). Prior to the L-PBF process, an in-depth analysis of temperature distribution and residual stress of samples was conducted using a multiphysics simulation tool (Materialise simulation, Materialise NV, Leuven, Belgium). Following a comprehensive preliminary study on residual stress prediction and the assessment of printing quality across various build angles ranging from 0° to 75°, a build angle of 60° (Figs. 3.2c and d) was ultimately selected. This specific angle was found to minimize lattice distortion caused by residual stress and reduce quality degradation resulting from overhang, as demonstrated in Figs. 3.2a and c.
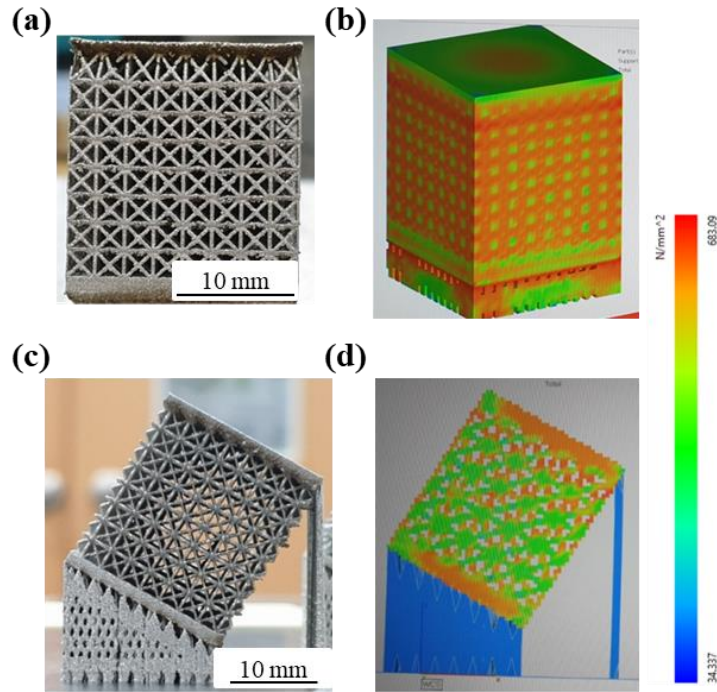
Figure 3.2. Different build orientations of FCCXYZ lattice structures. (a) Sample image and (b) residual stress distribution at 0°; (c) sample image and (d) residual stress distribution at 60°.

3.2.3. Compression test

Quasi-static compression tests were performed using a Universal Testing Machine (DTU900-MH, Daekyoung, Incheon, South Korea) equipped with a 300 KN load cell. The tests were conducted at room temperature with a constant crosshead speed of 1 mm/min, and each specimen underwent three replicate tests. Strain measurements were obtained using a laser extensometer (LX 500, MST, Minnesota, USA) with a gauge length of 20 mm. The engineering compressive stress for each lattice structure was calculated based on the initial cross-sectional area of the specimen (20×20 mm^2). In accordance with ASTM E9-09 [39], the compressive yield strengths were determined as the arithmetic mean of compressive stress at the plastic compressive strain of

0.2%. A video camera was utilized to record the deformation behavior during the compression process. Furthermore, the mechanical properties of each material were derived from tensile tests of AMed standard samples (following ASTM E8) as detailed in Table 3.3.

Table 3.3. Mechanical properties of AMed materials

Materials	Mass density (g/cm³)	Young's modulus (GPa)	Yield strength (MPa)	Tensile strength (MPa)	Elongation at break (%)
SUS316L	7.95	188±17	491±6	582±15	49±5
Tool steel 1.2709	8.00	181±2	1076±15	1213±20	10±2
Ti-Gr.2	4.43	111±3	577±5	703±5	25±2
AlSi10Mg	2.67	75±3	276±5	482±5	5±2

3.3. Results and discussion

3.3.1. Microstructure and density

The size of a specimen produced using the L-PBF method often deviates from the CAD model due to thermally induced deformation and powder particle adhesion near the melt pool [31,40]. This discrepancy in size relative to the original design is particularly noticeable on a small scale of approximately 300 µm, as considered in our study. In our investigation, we considered both the deviations in relative density (RD) from the original design and utilized optical microscopy (OM). Our findings revealed that as the strut size decreased, the error in RD generally increased (Table 3.4). Additionally, our RD measurements indicated that, for each sample, the actual relative density was slightly greater than the original design, with the most significant difference of 11.12% observed in tool steel 1.2709 samples with a strut diameter of 0.3 mm or 0.35 mm.

Table 3.4. RD comparison of printed FCCXYZ lattice structures

Strut diameter (mm)	Designed RD	SUS316L		Tool steel 1.2709		Ti-Gr.2		AlSi10Mg	
		Actual RD	Error (%)	Actual RD	Error (%)	Actual RD	Error (%)	Actual RD	Error (%)
0.30	0.11	0.119±0.002	7.40	0.123±0.004	11.12	0.123±0.013	10.78	0.120±0.009	8.36
0.35	0.15	0.156±0.004	6.94	0.162±0.003	11.12	0.160±0.017	9.43	0.162±0.008	10.96
0.40	0.19	0.199±0.007	7.79	0.203±0.005	9.66	0.196±0.016	5.88	0.205±0.007	10.94
0.45	0.23	0.241±0.008	6.31	0.246±0.003	8.28	0.241±0.011	6.08	0.250±0.005	10.06
0.50	0.27	0.285±0.011	5.25	0.292±0.010	7.59	0.283±0.024	4.31	0.297±0.006	9.44
0.55	0.32	0.330±0.009	4.09	0.334±0.009	5.37	0.330±0.018	4.17	0.340±0.015	7.34
0.60	0.36	0.377±0.007	3.52	0.386±0.008	5.90	0.376±0.025	3.30	0.388±0.019	6.62

The geometry of the AMed lattice structure samples was analyzed using optical microscopy (OM). The FCCXYZ lattice structure, tool steel samples displayed rough surface morphologies on the bottom surfaces of x-, y-, and cross-struts, deviating from the expected relative density (RD). Additionally, the diameter distribution of vertical (z-) struts exhibited greater uniformity when compared to parallel (x, y-) and diagonal (xz, yz-) struts. It was noted that as the strut diameter increased, there was a significant decrease in surface roughness (Fig. 3.3b). Surface quality of micro-lattice structures is influenced by parameters such as the stair-step effect and powder adhesion [40,41]. The rough surface boundary observed in unsupported overhangs of the parallel (x, y-) struts has also been attributed to contributing to surface roughness.

In Figure 3.4, the microstructures of the additive manufacturing (AM) sample with SUS316L are depicted. As illustrated in Fig. 3.4a, characteristic shell-like boundaries, referred to as a melt pool, resulting from the L-PBF process were evident, spanning from 42 to 67 μm (Fig. 3.4b). Furthermore, a few entrapped pores within the textures were discernible in Fig. 3.4a.
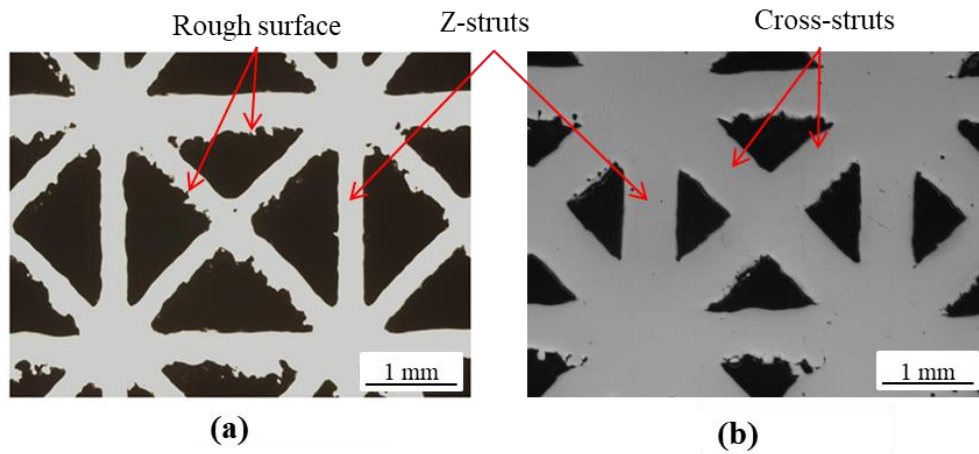
Figure 3.3. Optical micrographs of polished tool steel samples with FCCXYZ structure, (a) d=0.30 mm, (b) d=0.50 mm.
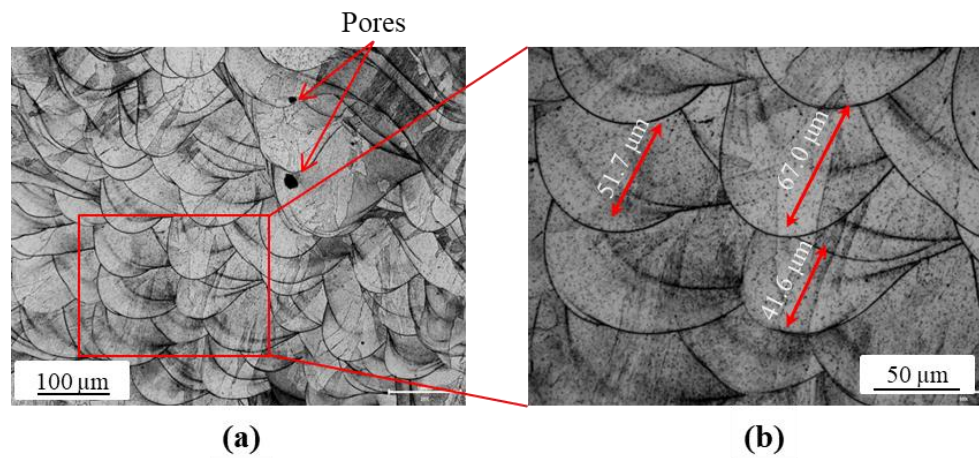
Figure 3.4. Optical micrographs of etched SUS316L samples with FCCXYZ structure.

3.3.2. Deformation behaviors and mechanical properties

The study focuses on analyzing the relationship between the structural factors and mechanical properties of AM samples with varying RD. Each strut plays a crucial role as a load-bearing

component in the lattice structures, and any changes in RD directly impact the mechanical properties and deformation behaviors of the FCCXYZ lattice structure. The engineering stress-strain curves of FCCXYZ lattice structures from quasi-static compression tests are depicted for each material with different RDs in Fig.3.5. To maintain clarity, a single representative curve for each set of experiments is chosen for display. The deformation process of the lattice structures is characterized by three stages: linear elasticity, plateau, and densification. In the initial stage, the FCCXYZ lattice structures exhibit elastic deformation, with stress increasing linearly up to the yield point. The subsequent plateau stage is influenced by the yield stress, buckling, and rupture of struts in the unit cell structures. Finally, in the third stage, stress rapidly increases as struts are pressed closely together to form a densified region. With increasing RD, the stiffness and plateau strength of the FCCXYZ lattice structure consistently increase, while the densification strain decreases (Fig. 3.5).

The distinctive pattern observed in the plateau for low RDs depicted in Fig. 3.5 can be ascribed to the gradual failure of individual layers. In the base materials investigated in the current study, except for SUS316L, the deformation mode (as shown in Fig. 3.6) with an RD of 0.11 (corresponding to a strut diameter of 0.3 mm and a resulting d/l of 0.12) occurred due to the progressive collapse of layers. When the struts are slender (a small d/l, i.e., a low RD), they tend to buckle prior to reaching the yield stress. For an RD of 0.11, the failure modes of FCCXYZ lattice structures under compression predominantly involved the bending of diagonal (xz,yz-) struts and the buckling of vertical (z-) struts. The parallel (x,y-) struts, untouched during compression, act as boundaries separating the layers in the structure, leading to the independent structural collapse of each layer.
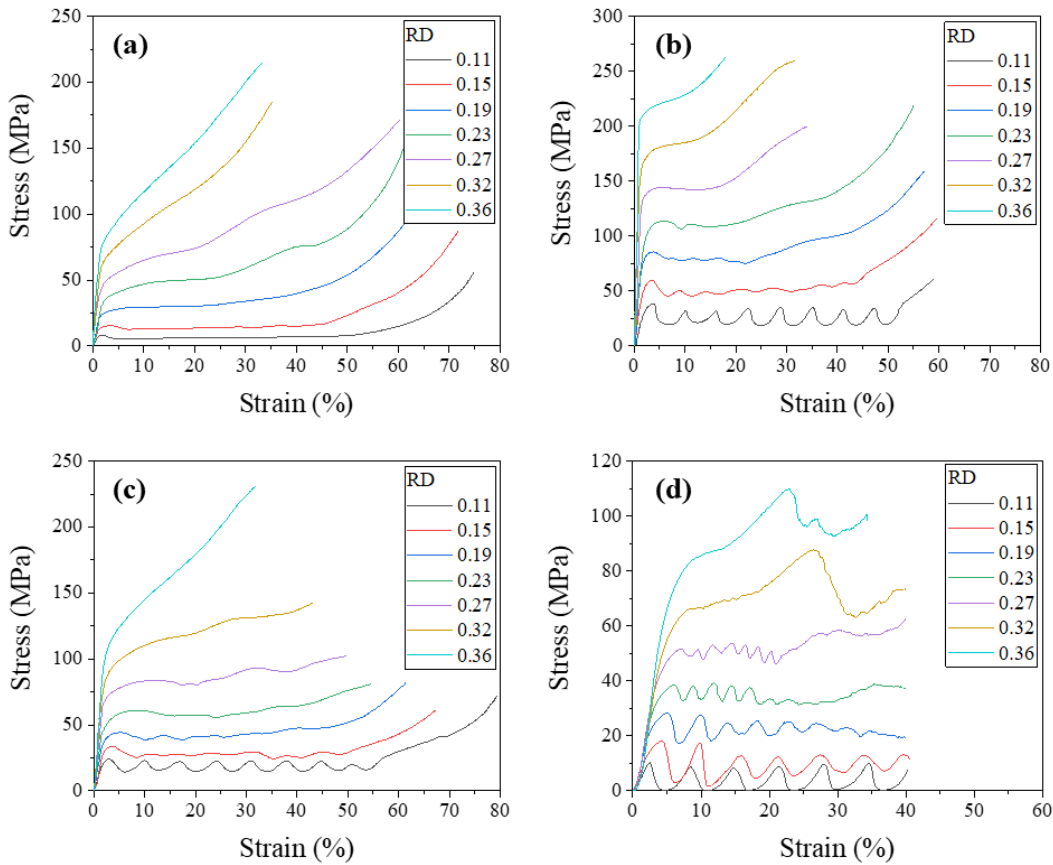
Figure 3.5. Experimental stress-strain curves of FCCXYZ lattice structures with various densities: (a) SUS316L, (b) tool steel 1.2709, (c) Ti-Gr2, and (d) AlSi10Mg.

A relatively high RD (for example, an RD of 0.36) resulted in the indistinct plateau stage of the tested structures. When the strain reached 27% for RD=0.32 and 24% for RD=0.36, the stress-strain curves of the AlSi10Mg lattice structure showed a rapid decline. This decline was due to a 45° inclined fracture in the AlSi10Mg structure, as illustrated in Fig. 3.7, which resembled the deformation pattern observed in compressive fractures of brittle bulk material. The primary cracks predominantly extended along the 45° direction.

Strain-stress curves with numerous ripples were observed at different RD ranges for each material (SUS316L: none; tool steel: 0.11-0.15; Ti-Gr.2: 0.11-0.19; AlSi10Mg: 0.11-0.27), as

shown in Fig. 3.5. This indicates that the stress-strain curves of lattice structures at low RDs exhibit distinct features depending on the mechanical properties, notably the ductility, of the base material. The most ductile material (SUS316L) exhibited long plateaus without ripples, while other materials exhibited ripples in the plateau stage, particularly at low RDs. It's worth noting that the tool steel (elongation: ~10%), Ti-Gr.2 (elongation: ~25%), and AlSi10Mg (elongation: ~5%) showed significantly lower ductility compared to the SUS316L (elongation: ~49%).
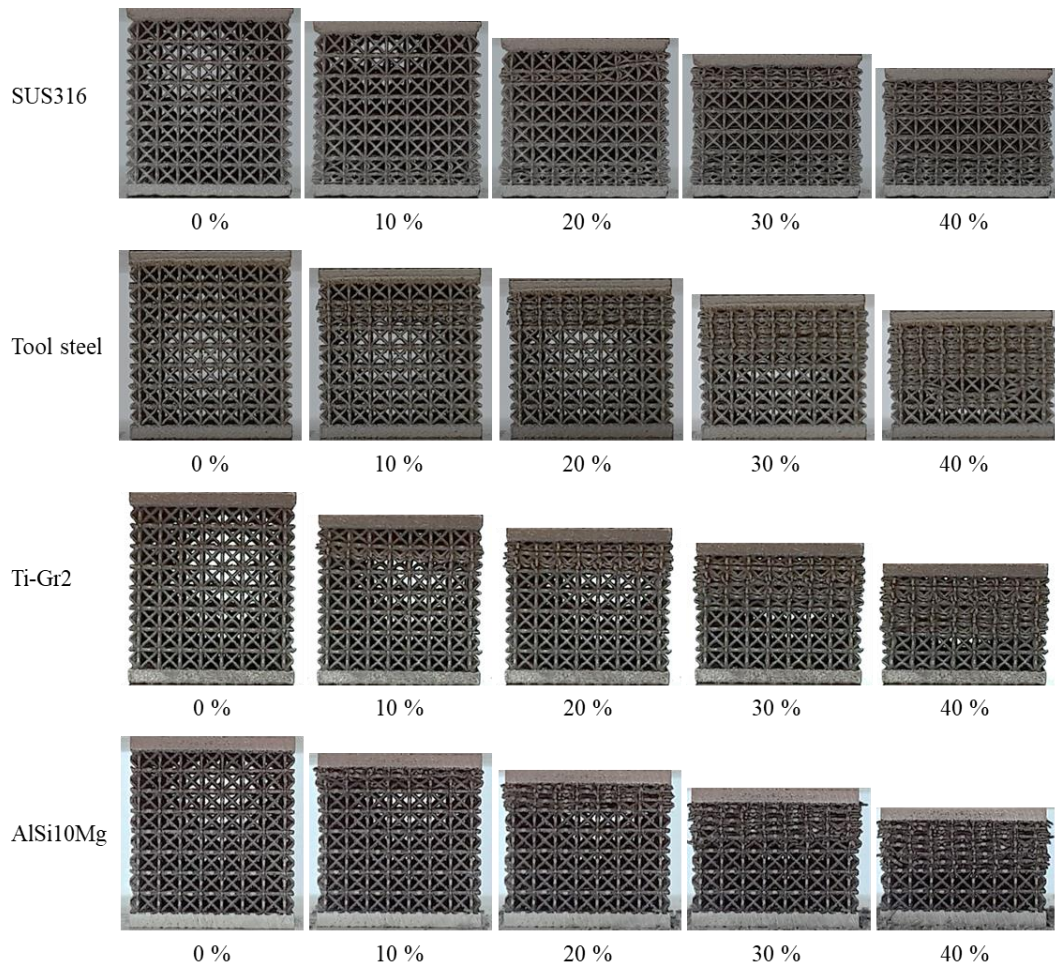
Figure 3.6. Deformation behaviors of FCCXYZ samples with strut diameter of 0.30 mm under compression loading. The bottom numbers denote strains.
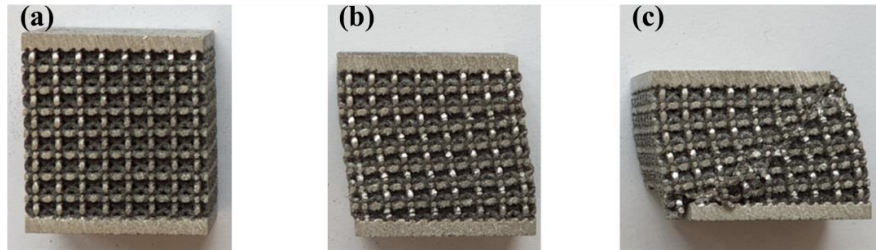
Figure 3.7. Deformation behaviors of AlSi10Mg samples with RD of 0.32 under compression loading: (a) 10 %, (b) 20%, and (c) 40%.

3.3.3. Methodology for lattice structure design

In this section, we will discuss the design of a lattice structure based on our experimental results. Firstly, we will examine the basic response behavior to stress based on the truss shape, specifically the FCCXYZ unit cell. This has implications for the selection of RD and materials to achieve the desired mechanical properties. Lastly, we will plot energy absorption as a function of RD to provide fundamental information for designing an energy-absorption structure.

3.3.3.1 Design of lattice structure: Maxwell stability criterion

The deformation mechanism of open-cell structures is heavily contingent upon their structure and the interconnection of their struts [43,44]. The use of Maxwell's stability criteria is instrumental in determining whether the deformation behavior is bending-dominated or stretching-dominated. In the context of 3D structures, the Maxwell stability criterion is expressed as:

$$M = s - 3j + 6 \qquad (3)$$

where M is the Maxwell stability number, and *s* and *j* are the numbers of struts and joints, respectively. For this specific unit cell, the calculation yields a value of 0 for M, indicating that the FCCXYZ structure exhibits stretching-dominated behavior, wherein individual struts experience stretching under a compressive load. This results in an effective distribution of internal stress, contributing to superior modulus and strength compared to a bending-dominated structure with the same relative density (RD). As a result, stretch-dominated lattice structures are deemed highly promising for lightweight structural applications. It is important to note, however, that stretching-dominated structures exhibit a post-yield softening response due to the buckling of the struts in compression. On the contrary, bending-dominated structures demonstrate a superior specific energy absorption behavior, characterized by a long stress plateau under compression [44].

3.3.3.2. Prediction of mechanical properties: Gibson-Ashby model

In general, the mechanical properties of lattice structures depend on their RD (ρ^*/ρ_s). The relations between mechanical properties and RD have been suggested by Gibson-Ashby with coefficients (C_1 and C_2) and exponents (*m* and *n*) for the lattice structures, as presented:

$$\frac{E^*}{E_s} = C_1 \left(\frac{\rho^*}{\rho_s}\right)^m \qquad (4)$$

$$\frac{\sigma^*}{\sigma_s} = C_2 \left(\frac{\rho^*}{\rho_s}\right)^n \qquad (5)$$

where E^*, σ^* and ρ^*denote the elastic modulus, yield strength, and density of a lattice structure, respectively, as summarized in Table 3.5. Similarly, E_s, σ_s, and ρ_s indicate the elastic modulus, yield strength, and density of the corresponding fully dense base material, respectively. The parameters C_1, C_1, m, and n are constants depending on the topology of unit cell. Based on the tensile test, E_s and σ_s were determined as given in Table 3.3.

Table 3.5. Mechanical properties of the investigated lattice structures

Material	Designed RD	Young's modulus (MPa)	Yield strength (MPa)	Energy absorption (MJ/m^3)
SUS316L	0.11	1643±19	7.8±2.0	1.8±0.5
	0.15	2912±18	13.3±1.7	4.0±0.5
	0.19	3937±51	21.7±2.4	8.7±1.1
	0.23	4562±27	28.0±3.2	13.9±1.6
	0.27	5750±46	44.5±2.2	20.6±1.2
	0.32	8272±67	54.3±4.8	31.3±2.8
	0.36	9044±72	73.6±3.4	40.1±1.9
Tool steel 1.2709	0.11	1852±48	38.4±3.2	7.4±0.6
	0.15	2927±15	57.4±4.8	14.8±1.3
	0.19	3608±61	80.6±6.1	23.7±1.8
	0.23	4596±32	97.3±8.5	33.2±2.9
	0.27	8300±43	133.3±9.6	45.5±3.3
	0.32	10191±42	162.8±10	61.2±3.8
	0.36	12047±74	204.6±11	-
Ti-Gr.2	0.11	1249±13	21.7±1.8	5.3±0.4
	0.15	1357±20	29.9±1.6	8.1±0.7
	0.19	2259±25	37.4±2.2	11.9±0.9
	0.23	2692±63	47.0±3.5	16.7±1.5
	0.27	3817±32	67.3±3.1	23.8±1.7

	0.32	4660±56	79.8±2.6	33.1±2.1
	0.36	5629±29	97.2±4.8	47.5±2.6
	0.11	467±11	9.5±1.2	1.08±0.2
	0.15	791±14	14.3±0.8	2.68±0.2
	0.19	1022±15	26.2±2.6	6.5±0.6
AlSi10Mg	0.23	1364±13	32.2±3.2	9.6±1.1
	0.27	1725±18	41.5±4.5	14.2±1.5
	0.32	2164±20	52.3±5.4	19.6±2.0
	0.36	2727±39	61.4±7.8	24.7±3.1

In Figure 3.8, the log-log plots depict the relative modulus and relative yield strength of FCCXYZ lattice structures plotted against their RDs based on experimental results. The Gibson-Ashby model's parameters (C_1, C_2, m, and n) were determined through fitting equations to the experimental results, as outlined in Table 3.6. The correlation degree (R^2) for the entire experimental dataset exhibited high values for both modulus (>0.96) and strength (>0.98). The coefficients (C_1, C_2) for the modulus of the FCCXYZ lattice structure with various materials fall within the range of 0.21-0.33, while the coefficients for yield strength fall within the range of 0.59-0.89. These values validate previous findings by Gibson-Ashby, which established that the coefficients for metallic open-cell cellular structures typically range from 0.1-4 for the modulus and 0.1-1 for the yield strength. [14]
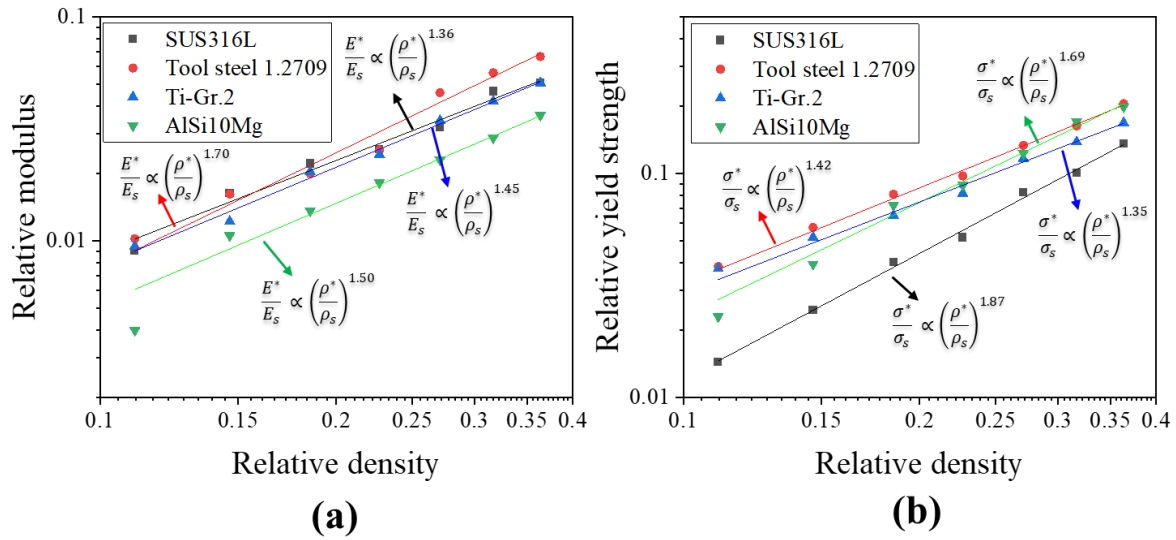
Figure 3.8. The relative modulus and relative compressive yield strength as a function of RD on the Gibson-Ashby chart.

Table 3.6. The parameters of the Gibson-Ashby model for modulus and Yield strength

Materials	Young's modulus (MPa)			Yield strength (MPa)		
	Coefficient (C_1)	Exponent (m)	Correlation (R^2) %	Coefficient (C_2)	Exponent (n)	Correlation (R^2) %
SUS316L	0.22	1.36	97.94	0.89	1.87	99.52
Tool steel 1.2709	0.33	1.70	97.76	0.80	1.42	99.65
Ti-Gr.2	0.22	1.45	99.51	0.59	1.35	99.18
AlSi10Mg	0.21	1.50	98.76	0.85	1.69	98.73

In the passage, we explored the representation of mechanical properties in lattice structures through the application of equations put forth by Gibson-Ashby. These equations establish a correlation between the relative density (RD) of the structure and the properties of the parent material [14,44]. The properties in question are contingent upon the structural response,

distinguishing between bending-dominated and stretching-dominated behavior, and are intrinsically linked to the relative density of the structures. Within the framework of the Gibson-Ashby model, the exponent values (denoted as *m* and *n*) delineate the overarching behavior of the structures in relation to bending- or stretching-dominated characteristics. Notably, for bending-dominated structures, the exponent values are 2 for modulus (*m*) and 1.5 for strength (*n*), whereas stretching-dominated structures are characterized by exponent values of 1.0 for both modulus and strength.

Our empirical findings indicate that the exponent values of FCCXYZ lattice structures are contingent upon the material under consideration. The experimental values for modulus ranged from 1.36 to 1.70, while the strength values were observed to fall within the range of 1.35 to 1.87. Despite FCCXYZ being characterized as a structure primarily subjected to stretching, as per the Maxwell criterion, the exponents derived from the experiment predominantly exhibit characteristics that align with both bending- and stretching-dominated behaviors ($1<m<2$ and $1<n<1.5$).

The congruence of our experimental results with the Gibson-Ashby model attests to the model's applicability in analyzing and prognosticating the behavior of AMed lattice structures. Moreover, the coefficients and exponent values computed based on the Gibson-Ashby model can function as crucial references for designing lattice structures, considering the materials employed in the current investigation. While achieving wholly precise predictions of these properties may be unattainable, the Gibson-Ashby model is deemed valuable in facilitating acceptable structural design and material selection. The marginal disparities between the empirical results of this study and the Gibson-Ashby model may be ascribed to several factors. For instance, the presence of unmelted powder adhering to the surface of printed components contributes to an increase in

weight without a corresponding increase in volume, leading to miscalculations of the relative density and deviations from the anticipated results. Additionally, residual stresses stemming from AM fabrication can precipitate deformations at lower stress levels than anticipated.

3.3.3.3. Calculation of specific energy absorption (SEA)

An essential and widely employed parameter for characterizing lattice structures involves their energy absorption capacity (EA) [14]. Energy absorption (EA) is specifically defined as the absorbed energy per unit volume of the lattice structure. The determination of EA up to 30% strain was documented as [39]:

$$W = \int_0^{\varepsilon_0} \sigma d\varepsilon \tag{6}$$

where W is the energy absorption per unit volume (J/m^3); σ is the compressive stress (Pa); ε_0 is the strain at a specific moment in the compression process (ε_0=0.3). The ideal specific energy absorption (SEA) is the ratio of energy absorbed during compression (up to 30% strain) to the cellular density (ρ^*) of the lattice structure. The specific energy absorption can be determined using the formula:

$$SEA = \frac{W}{\rho^*} \tag{7}$$

Figure 3.9 presents the SEA of the FCCXYZ lattice structures in relation to RD. A lattice structure characterized by a high RD exhibits superior mechanical properties and specific energy

absorption capabilities. Prior research has demonstrated that the relationship between SEA and RD can be linear or exhibit higher scale tendencies, contingent upon the geometry of the lattice structure and the mode of deformation [14,26,32]. Our study indicates that, for the selected FCCXYZ structure (Fig. 3.9), the relationship between SEA and RD follows a monotonically increasing function (linear function). In the FCCXYZ structure, a higher RD yields a notable increase in energy absorption efficiency.
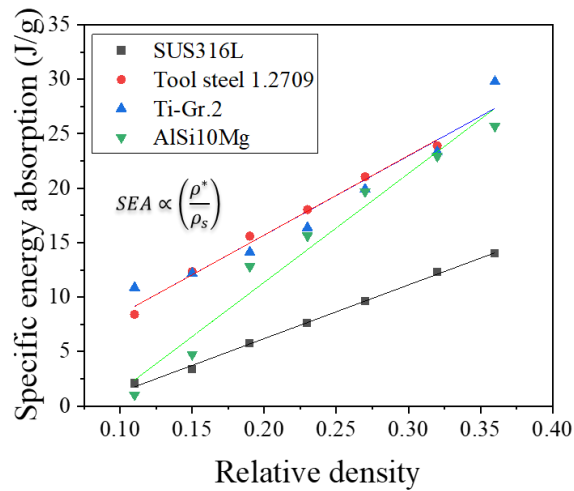
Figure 3.9. The specific energy absorption (SEA) of FCCXYZ lattice structures after 30% compression strain as a function of RD in the range between 11% and 36%.

Tool steel demonstrated superior load-carrying capacity and high work-hardening capacity, resulting in favorable specific energy absorption (SEA) across the range of relative densities (RDs) studied. When comparing the lattice structures of Ti-Gr.2 and SUS316L, it was observed that, although the SUS316L and Ti-Gr.2 structures displayed similar strength, Ti-Gr.2 was 45% lighter than SUS316L. Consequently, the SEA of the Ti-Gr.2 structure was found to be comparable to that of tool steel and nearly double that of the SUS316L structure. Among the materials examined,

AMed AlSi10Mg exhibited the lowest yield strength. Despite this, owing to its advantageous lightweight property, the SEA of the AlSi10Mg structure closely approximated that of Ti-Gr.2 or tool steel at high relative densities. Thus, these findings suggest that material selection and relative density can be customized to achieve an optimal combination of properties for a specific lattice structure.

3.4. Conclusions

In this study, we investigated the influence of material type and relative density (RD) on the mechanical properties of the FCCXYZ lattice structure in various metallic materials (SUS316L, tool steel 1.2709, Ti-Gr.2, and AlSi10Mg) using quasi-static compression tests.

Our findings indicate that the failure mechanism of the FCCXYZ lattice structure, whether it involves progressive collapse of layers or bulky collapse, is contingent upon the material type and RD. Furthermore, we observed that at the same RD, the failure mechanism can vary based on the specific material characteristics.

Interestingly, our study revealed that the FCCXYZ lattice structure exhibits a nuanced interplay between stretching- and bending-dominated behaviors across all materials, even though it was expected to be a stretching-dominated structure.

Moreover, we discovered that the specific energy absorption (SEA) of the Ti-Gr.2 structure is comparable to that of tool steel 1.2709, while the AlSi10Mg structure demonstrates notably high SEA at high RD. These fundamental insights will have significant implications for the design of energy absorption systems using metal additive manufacturing.

References

[1] Buchanan C, Gardner L. Metal 3D printing in construction: A review of methods, research, applications, opportunities and challenges. Eng Struct 2019; 180:332–48.

[2] Spalt P, Bauernhansl T. A Framework for Integration of Additive Manufacturing Technologies in Production Networks. Proc CIRP 2016; 57:716–21.

[3] Maconachie T, Leary M, Lozanovski B, Zhang X, Qian M, Faruque O, et al. SLM lattice structures: Properties, performance, applications and challenges. Mater Des 2019; 183:108137.

[4] Chu C, Graf G, Rosen DW. Design for Additive Manufacturing of Cellular Structures. Comput-Aided Des Appl 2008; 5:686–96.

[5] Gibson I, Rosen D, Stucker B. Additive Manufacturing Technologies: 3D Printing, Rapid Prototyping, and Direct Digital Manufacturing. New York, NY: Springer New York; 2015.

[6] Sames WJ, List FA, Pannala S, Dehoff RR, Babu SS. The metallurgy and processing science of metal additive manufacturing. Int Mater Rev 2016; 61:315–60.

[7] Domfang Ngnekou JN, Nadot Y, Henaff G, Nicolai J, Ridosz L. Influence of defect size on the fatigue resistance of AlSi10Mg alloy elaborated by selective laser melting (SLM). Procedia Struct Integr 2017; 7:75–83.

[8] Poprawe R, Hinke C, Meiners W, Schrage J, Bremen S, Merkt S. SLM Production Systems: Recent Developments in Process Development, Machine Concepts and Component Design. In: Brecher C, editor. Advances in Production Technology, Cham: Springer International Publishing; 2015, p. 49–65.

[9] Yuan L, Ding S, Wen C. Additive manufacturing technology for porous metal implant applications and triple minimal surface structures: A review. Bioact Mater 2019; 4:56–70.

[10] Majeed A, Ahmed A, Salam A, Sheikh MZ. Surface quality improvement by parameters analysis, optimization and heat treatment of AlSi10Mg parts manufactured by SLM additive manufacturing. Int J Lightweight Mater Manuf 2019; 2:288–95.

[11] Klahn C, Leutenecker B, Meboldt M. Design Strategies for the Process of Additive Manufacturing. Proc CIRP 2015; 36:230–5.

[12] Panesar A, Abdi M, Hickman D, Ashcroft I. Strategies for functionally graded lattice structures derived using topology optimisation for Additive Manufacturing. Addit Manuf

2018; 19:81–94.

[13] Fleck NA, Deshpande VS, Ashby MF. Micro-architectured materials: past, present and future. Proc R Soc A 2010; 466:2495–516.

[14] Gibson LJ, Ashby MF. Cellular Solids: Structure and Properties. 2nd ed. Cambridge University Press; 1997.

[15] Zadpoor AA. Mechanical performance of additively manufactured meta-biomaterials. Acta Biomater 2019; 85:41–59.

[16] Guo N, Leu MC. Additive manufacturing: technology, applications and research needs. Front Mech Eng 2013;8:215–43.

[17] Sairajan KK, Aglietti GS, Mani KM. A review of multifunctional structure technology for aerospace applications. Acta Astronaut 2016; 120:30–42.

[18] Alabort E, Barba D, Reed RC. Design of metallic bone by additive manufacturing. Scr Mater 2019; 164:110–4.

[19] Yang D-H, Shang-Run Y, Hui W, Ai-Bin M, Jing-Hua J, Jian-Qing C, et al. Compressive properties of cellular Mg foams fabricated by melt-foaming method. Mater Sci Eng A 2010; 527:5405–9.

[20] Jinnapat A, Kennedy AR. The manufacture of spherical salt beads and their use as dissolvable templates for the production of cellular solids via a powder metallurgy route. J Alloys Comd 2010;499:43–7.

[21] Nannan C, Yi F, Jie C, Bin L, Fanyan C, Jingsong Z. Vacuum Brazing Processes of Aluminum Foam. Rare Metal Mater Eng 2013; 42:1118–22.

[22] Vendra LJ, Rabiei A. A study on aluminum–steel composite metal foam processed by casting. Mater Sci Eng A 2007; 465:59–67.

[23] Maskery I, Aboulkhair NT, Aremu AO, Tuck CJ, Ashcroft IA, Wildman RD, et al. A mechanical property evaluation of graded density Al-Si10-Mg lattice structures manufactured by selective laser melting. Mater Sci Eng A 2016; 670:264–74.

[24] Al-Saedi DSJ, Masood SH, Faizan-Ur-Rab M, Alomarah A, Ponnusamy P. Mechanical properties and energy absorption capability of functionally graded F2BCC lattice fabricated by SLM. Mater Des 2018; 144:32–44.

[25] Chen B, Moon SK, Yao X, Bi G, Shen J, Umeda J, et al. Strength and strain hardening of a selective laser melted AlSi10Mg alloy. Scr Mater 2017; 141:45–9.

[26] Köhnen P, Haase C, Bültmann J, Ziegler S, Schleifenbaum JH, Bleck W. Mechanical properties and deformation behavior of additively manufactured lattice structures of stainless steel. Mater Des 2018; 145:205–17.

[27] Hedayati R, Sadighi M. A micromechanical approach to numerical modeling of yielding of open-cell porous structures under compressive loads. Jtam 2016:769.

[28] Choy SY, Sun C-N, Leong KF, Wei J. Compressive properties of functionally graded lattice structures manufactured by selective laser melting. Mater Des 2017; 131:112–20.

[29] Yan C, Hao L, Hussein A, Young P, Raymont D. Advanced lightweight 316L stainless steel cellular lattice structures fabricated via selective laser melting. Mater Des 2014; 55:533–41.

[30] Li C, Lei H, Liu Y, Zhang X, Xiong J, Zhou H, et al. Crushing behavior of multi-layer metal lattice panel fabricated by selective laser melting. Int J Mech Sci 2018; 145:389–99.

[31] Mazur M, Leary M, McMillan M, Sun S, Shidid D, Brandt M. Mechanical properties of Ti6Al4V and AlSi12Mg lattice structures manufactured by Selective Laser Melting (SLM). Laser Additive Manufacturing, Elsevier; 2017, p. 119–61.

[32] Xiao Z, Yang Y, Xiao R, Bai Y, Song C, Wang D. Evaluation of topology-optimized lattice structures manufactured via selective laser melting. Mater Des 2018; 143:27–37.

[33] Smith M, Guan Z, Cantwell WJ. Finite element modelling of the compressive response of lattice structures manufactured using the selective laser melting technique. Int J Mech Sci 2013; 67:28–41.

[34] Han C, Li Y, Wang Q, Wen S, Wei Q, Yan C, et al. Continuous functionally graded porous titanium scaffolds manufactured by selective laser melting for bone implants. J Mech Behav Biomed Mater 2018; 80:119–27.

[35] Yan C, Hao L, Hussein A, Raymont D. Evaluations of cellular lattice structures manufactured using selective laser melting. Int J Mach Tools Manuf 2012; 62:32–8.

[36] Li Z, Nie Y, Liu B, Kuai Z, Zhao M, Liu F. Mechanical properties of AlSi10Mg lattice structures fabricated by selective laser melting. Mater Des 2020; 192:108709.

[37] Mazur M, Leary M, McMillan M, Elambasseril J, Brandt M. SLM additive manufacture of H13 tool steel with conformal cooling and structural lattices. RPJ 2016; 22:504–18.

[38] Katancik M, Mirzababaei S, Ghayoor M, Pasebani S. Selective laser melting and tempering of H13 tool steel for rapid tooling applications. J Alloys Compd 2020;

849:156319.

[39] E28 Committee. Test Methods of Compression Testing of Metallic Materials at Room Temperature. ASTM International; n.d.

[40] Echeta I, Feng X, Dutton B, Leach R, Piano S. Review of defects in lattice structures manufactured by powder bed fusion. Int J Adv Manuf Technol 2020; 106:2649–68.

[41] Leary M, Mazur M, Elambasseril J, McMillan M, Chirent T, Sun Y, et al. Selective laser melting (SLM) of AlSi12Mg lattice structures. Mater Des 2016; 98:344–57.

[42] Emmelmann C, Herzog D, Kranz J. Design for laser additive manufacturing. Laser Additive Manufacturing, Elsevier; 2017, p. 259–79.

[43] Deshpande VS, Fleck NA, Ashby MF. Effective properties of the octet-truss lattice material. J Mech Phys of Solids 2001; 49:1747–69.

[44] Ashby MF. The properties of foams and lattices. Phil Trans R Soc A 2006; 364:15–30.

[45] Gibson, I., Rosen, D. & Stucker, B. Additive Manufacturing Technologies: 3D Printing, Rapid Prototyping, and Direct Digital Manufacturing. (Springer New York, New York, NY, 2015). doi:10.1007/978-1-4939-2113-3.

[46] Altan, T., Lilly, B., Yen, Y. C. & Altan, T. Manufacturing of Dies and Molds. CIRP Annals 50, 404–422 (2001).

[47] S.N.A. Shahbudin, M.H. Othman, S.Y.M. Amin, M.H.I. Ibrahim, A review of metal injection molding- Process, optimization, defects and microwave sintering on WC-Co cemented carbide IOP Conf. Ser. Mater. Sci. Eng., 226 (2017), Article 012162.

[48] E. Sachs, E. Wylonis, S. Allen, M. Cima, H. Guo (2000) Production of Injection Molding Tooling With Conformal Cooling Channels Using the Three Dimensional Printing Process, Polymer Eng. And Sci, Vol. 40.

[49] M. Mazur, P. Brincat, M. Leary, M. Brandt (2017) Numerical and experimental evaluation of a conformally cooled H13 steel injection mould manufactured with selective laser melting. Int. J. Adv. Manuf. Technol., 93, pp. 881–900.

[50] Chantzis, D. et al. Review on additive manufacturing of tooling for hot stamping. Int J Adv Manuf Technol 109, 87–107 (2020).

[51] Garrett, B. 3D Printing: New Economic Paradigms and Strategic Shifts. Global Policy 5, 70–75 (2014).

[52] Weller, C., Kleer, R. & Piller, F. T. Economic implications of 3D printing: Market structure models in light of additive manufacturing revisited. International Journal of Production Economics 164, 43–56 (2015).

[53] Asnafi, N., Rajalampi, J. & Aspenberg, D. Design and Validation of 3D-Printed Tools for Stamping of DP600. IOP Conf. Ser.: Mater. Sci. Eng. 651, 012010 (2019).

[54] Li, R. et al. Additive manufacturing (AM) of piercing punches by the PBF method of metal 3D printing using mold steel powder materials. J Mech Sci Technol 33, 809–817 (2019).

[55] Saby, M., Bouchard, P.-O. & Bernacki, M. Void closure criteria for hot metal forming: A review. Journal of Manufacturing Processes 19, 239–250 (2015).

[56] Ismail, A., Mohamed, M. S. Review on sheet metal forming process of aluminium alloys. 17th International Conference on Applied Mechanics and Mechanical Engineering. pp. 19–21 (2016).

[57] Taylor, T., Clough, A. Critical review of automotive hot-stamped sheet steel from an industrial perspective. Mater Sci Technol 34:809–861 (2018).

[58] S.A. Jahan, T. Wu, Y. Zhang, H. El-Mounayri, A. Tovar, J. Zhang, D. Acheson, R. Nalim, X. Guo, W.H. Lee (2016) Implementation of conformal cooling & topology optimization in 3D printed stainless steel porous structure injection molds, Procedia Manuf. 5, 901–915.

[59] Park, H. S., & Dang, X. P. Design and simulation-based optimization of cooling channels for plastic injection mold. New Technologies-Trends, Innovations and Research, 2, 19-44

(2012).

[60] Lin, Z.-C. & Chou, M.-H. Design of the cooling channels in nonrectangular plastic flat injection mold. Journal of Manufacturing Systems 21, 167–186 (2002).

[61] Cortina, M., Arrizubieta, J., Calleja, A., Ukar, E. & Alberdi, A. Case Study to Illustrate the Potential of Conformal Cooling Channels for Hot Stamping Dies Manufactured Using Hybrid Process of Laser Metal Deposition (LMD) and Milling. Metals 8, 102 (2018).

[62] Müller, B., Gebauer, M., Hund, R., Malek, R., & Gerth, N. Metal Additive Manufacturing for tooling applications-Laser Beam Melting technology increases efficiency of dies and molds. In Metal Additive Manufacturing Conference MAMC (2014).

[63] Wang, Y., Yu, K.-M., Wang, C. C. L. & Zhang, Y. Automatic design of conformal cooling circuits for rapid tooling. Computer-Aided Design 43, 1001–1010 (2011).

[64] Tan, C. et al. Design and additive manufacturing of novel conformal cooling molds. Materials & Design 196, 109147 (2020).

[65] Brooks, H. & Brigden, K. Design of conformal cooling layers with self-supporting lattices for additively manufactured tooling. Additive Manufacturing 11, 16–22 (2016).

CHAPTER IV

Cooling Performance of an Additively Manufactured Lattice Structural Conformal Cooling Channel for Hot Stamping

4.1 Introduction

In the hot stamping process, hot stamping steels (typically, alloyed with a certain amount of boron) are stamped at an elevated temperature to take advantage of reduced forming loads, enhanced ductility, and reduced springback [1]. After that, the stamped part is hardened by die quenching, thus improving its tensile strength. Therefore, the cooling performance is an essential factor affecting the productivity of the process.

Conventionally, cooling channels in hot stamping dies are formed by straight hole drilling [2]. As a result, the distance from the straight channels to the die surface in a complex shape varies, causing non-uniform heat transfer. Meanwhile, a concept of conformal cooling (CC) channels has been suggested to improve the cooling performance in injection molding of polymer products, in which the cooling channels are equally distanced from the die cavity surface [5,6]. With the recent development of metal additive manufacturing (AM) technology, the concept of CC channels is receiving interest from metal forming industries as a substitute for conventional straight-drilled cooling channels for hot stamping dies [7,8]. Also, the versatility of AM technology even allows the fabrication of CC channels filled with a lattice structure (a lattice structural CC channel), which reduces the weight of the dies while enhancing the cooling performance [9,10].

The lattice structural CC channel can simultaneously enhance the stiffness and cooling performance of a hot stamping die. Son *et al.* [11] considered the fluid flow and heat transfer of

lattice frame materials as a function of the Reynolds number in the laminar regime. Their results suggest that the lattice frame materials can provide heat transfer efficiency comparable to metal foams, while also incurring lower pressure drops and superior load capacity. Yun *et al.* [12] evaluated the effective thermal properties of a face-centered cubic with vertical struts lattice channels as a function of the porosity of the lattice structure. The optimal porosity of the lattice channel was determined by the evaluation of the thermal-structural performance factor. Au and Yu [13] suggested a scaffolding architecture for CC channel design with improved cooling performance. The cooling performance demonstrated that the scaffold cooling channel could offer a more uniform heat distribution and reduce injection mold defects such as warping and thermal stress.

The mechanical performance of a porous structure can be typically quantified based on the volume density of the structure [11,12,14]. Similarly, the design of a cooling channel (either straight or CC) with a lattice structure frequently has been based on the volume density of the lattice structure [12]. However, in heat transfer calculations, the surface area density affects performance of a porous structure [15]. Therefore, a lattice structural CC channel layout in a rapid cooling die for hot stamping should be adopted with consideration of both volume density and surface area density of the lattice structure.

In the present study, the performances of AMed lattice structural CC channels with different surface area densities and a constant volume density are experimentally compared to clarify the proper design principle for a hot stamping die with lattice structural CC channels. A simple computational fluid dynamics (CFD) analysis is also adopted to confirm the experimental result.

4.2 Design principle of CC channel with lattice structure

The conformal cooling (CC) channel was designed with a lattice structure incorporated within the dies (molds), as shown in Fig. 4.1. Lattice structures amplify heat transfer by augmenting the contact surface area and promoting turbulence in the coolant fluid. Additionally, they bolster mechanical strength and the manufacturability of additive manufacturing (AM) processes by reducing the span of overhang regions. However, the mechanical properties and cooling efficiency depend on the geometry and density of the lattice structure. This study examined the mechanical properties of three common structures: cross, honeycomb, and octahedral.
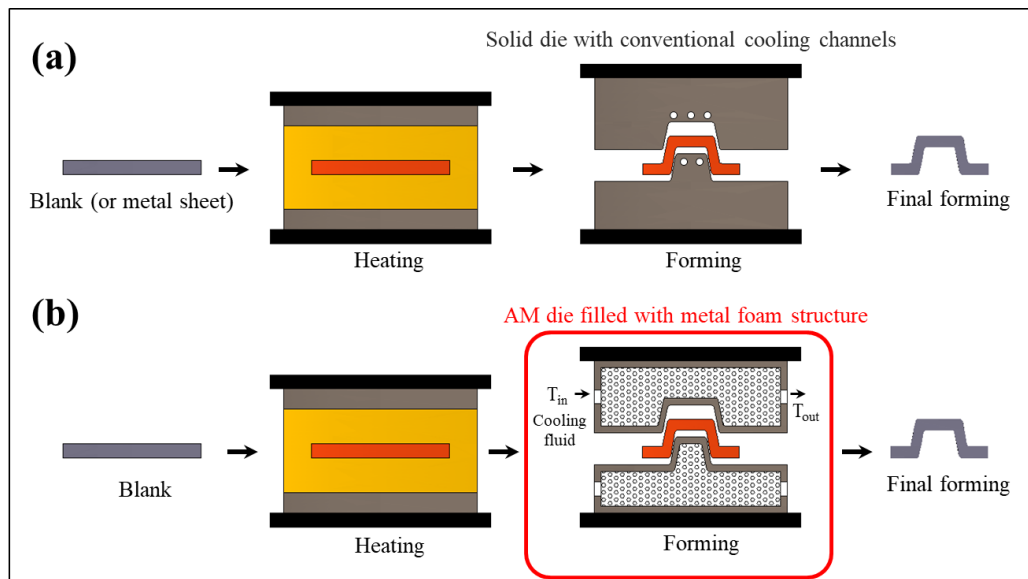

Figure 4.1. Design principle of CC channel (a) conventional (b) AM die filled with lattice structure.

A computer-aided design (CAD) software (Solidworks, Dassault Systèmes, Vélizy-Villacoublay, France) was employed to create lattice structures, including the cross, honeycomb, and octahedral shapes, as illustrated in Fig. 4.2 (a), (b), and (c). The primary unit cell with

dimensions of 2 mm × 2 mm × 2 mm was constructed using cylindrical cross-sectional struts. The strut diameter in each structure was adjusted to maintain a consistent density of 0.41. These lattice structures were created through 3D spatial repetition, resulting in external dimensions of 12 mm × 12 mm × 12 mm. Additionally, two solid panels were designed both below and above the lattice structure, as shown in Fig. 4.2.
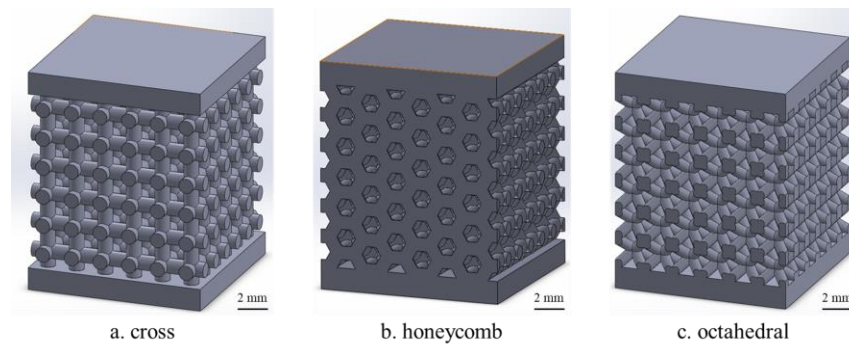
Figure 4.2. Schematics of the three lattice structures with the same RD=0.41: (a) cross, (b) honeycomb, (c) octahedral structure.

Finite Element Analysis (FEA) was conducted using ABAQUS 2017 software (Dassault Systèmes Simulia Corp., USA) to compare the stress fields under uniaxial compression for the three different structures within their elastic range. Numerical simulations were performed using static structural analysis to study each structure. The geometry of the structures was imported from the Solidworks database as STEP files. The cross, honeycomb, and octahedral geometry models have the exact dimensions specified in the design (height = 14 mm, thickness = 12 mm, and width = 12 mm). The elastic components listed in Table 4.1 were utilized as input parameters for the material simulation using the linear elastic material model, which includes density, Young's modulus, and Poisson's ratio derived from the supplier's specifications. Various mesh sizes were

compared to assess mesh quality. The lower face plate was fixed, and a reference point was placed in the middle of the upper face plate to apply the displacement. Additionally, the reaction force was determined from this reference point to compare the mechanical properties of the three types of structures.

Table 4.1. Mechanical properties of tool steel 1.2709

Materials	Mass density (g/cm³)	Young's modulus (GPa)	Poisson's ratio	Yield strength (MPa)
Tool steel 1.2709	8.00	181±2	0.3	1076±15

Figures 4.3 (b), (c), and (d) show the stress distribution in the cross, honeycomb, and octahedral structures. The simulation images reveal that stress is localized at the nodes and z-struts, which makes them the weak points at which fracture is initiated. Under the same loading conditions, each structure (at the same RD=0.41) deforms to a different extent, depending on the stiffness (or modulus) of the specific structure type.
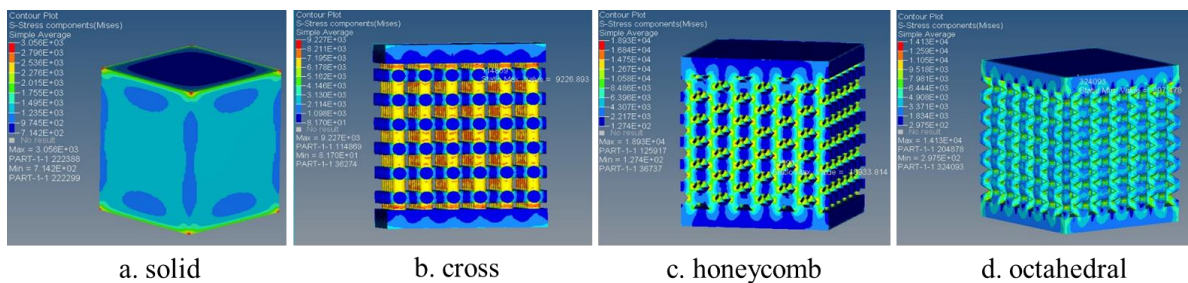

a. solid   b. cross   c. honeycomb   d. octahedral

Figure 4.3. Numerical results of stress components for three different lattice structures: (a) solid, (b) cross, (c) honeycomb, (d) octahedral.
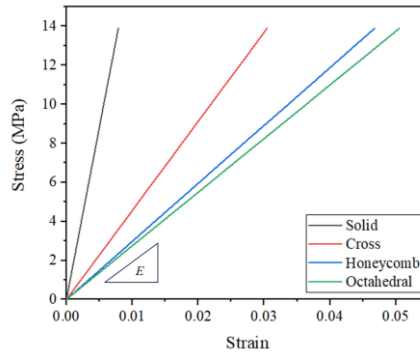
Figure 4.4. The stress-strain curve was obtained from the FEA results of three lattice structures in the elastic deformation region.

Table 4.2. Stiffness and surface area of the three lattice structures with the same RD=0.41

Structures	Relative density	Stiffness (modulus)	Surface area (mm^2)
Cross		**0.26E$_{soild}$**	**3407.17**
Honeycomb	0.41	0.17E$_{soild}$	3635.52
Octahedral		0.16E$_{soild}$	4254.84

Figure 4.4 shows the stress-strain curve obtained from the FEA results of the three lattice structures in the elastic deformation region. Young's modulus is highest for the cross structure (45.6 GPa), followed by the honeycomb structure (29.6 GPa), and then the octahedral structure (27.4 GPa). The cross structure with z-struts arranged in the loading direction enhances the stiffness (or modulus) of the structure. The cross structure exhibits a slightly smaller surface area than the other two structures, yet its stiffness surpasses that of the other two structures by approximately 1.5 times (as depicted in Table 4.2). Therefore, in this study, the cross structure is employed to design the hot stamping die to guarantee the die's mechanical properties.

4.3. Experimental set-up

4.3.1. AM of a cross lattice structure

A lab-scale hot stamping die with a CC channel filled with a simple cross lattice structure (Fig. 4.5) was fabricated by selective laser melting (SLM) using a custom-made AM machine (SLM 280HL, SLM Solutions Group AG, Germany) with 1.2709 tool steel powder (AMTM A646). The powder particles ranged in size from 10 µm to 45 µm. The SLM process is carried out in an argon gas chamber. The argon gas content was above 99.9%, and the flow velocity was set at approximately 22 m/s. The process parameters (Table 4.3) were selected to produce bulk and lattice structure samples with a high density (>99.6%). A scanning strategy with a contour hatch pattern and rotation of 67° between subsequent layers was chosen.
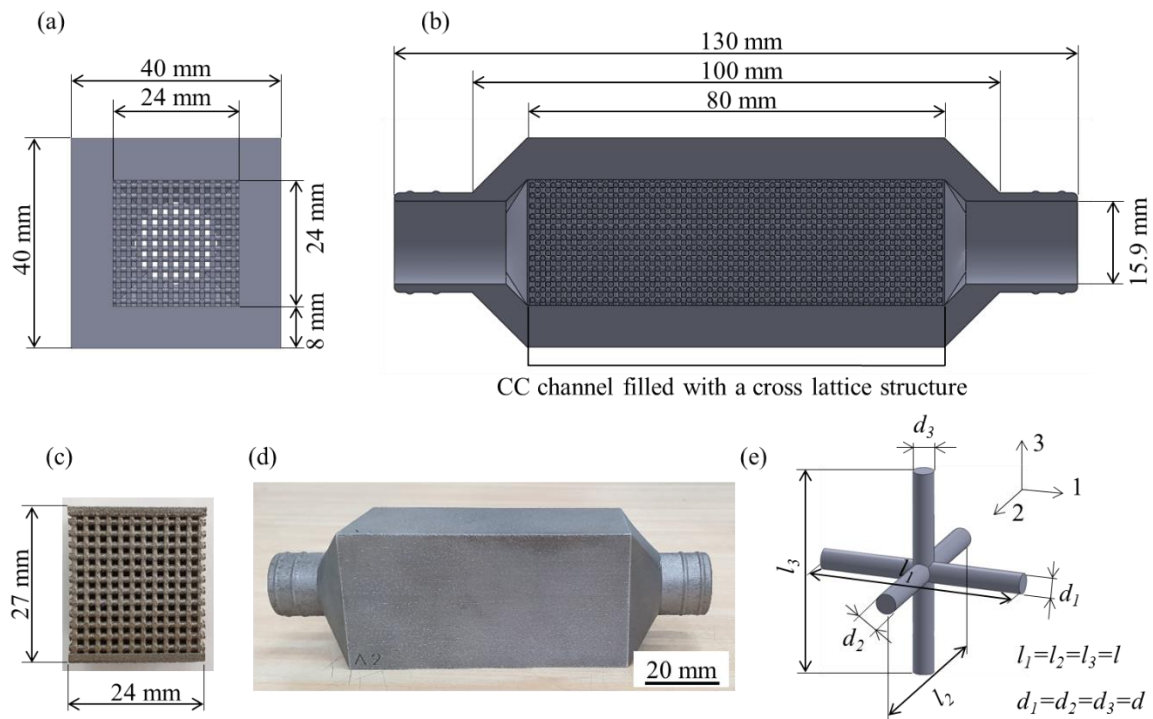

Figure 4.5. Pictures of (a) front view, (b) right view, (c) lattice structure sample (case III), (d) actual sample of the lab-scale hot stamping die, and (e) unit cell of cross structure.

Table 4.3. SLM process parameters

Laser power (W)	Hatch distance (μm)	Speed (mm/s)	Layer thickness (μm)
180	120	850	30

For the simple cross lattice structure selected in the present study (Fig. 4.5(e)), the relative density (RD) can be calculated as [14]

$$\frac{\rho_v}{\rho_s} = \frac{3\pi}{4}\left(\frac{d}{l}\right)^2 - C\left(\frac{d}{l}\right)^3 \tag{1}$$

where ρ_v and ρ_s are the volume density of structure and the density of solid material, respectively. Also, d and l represent the strut diameter and the edge length of unit cell, respectively (Fig. 4.5(d)). In Eqn. (1), the geometrical fitting parameter $C=1.41$ was adopted to consider the volume of the joint in the cross lattice structure. Also, for a given lattice structure, the surface area density ρ_A can be calculated from the surface area per unit volume of cross lattice structures (with the unit of m$^-$ ^{1}) as [16]

$$\rho_A = \frac{Surface\ area}{V} = 3\pi\frac{d}{l^2} - 6\sqrt{2}\frac{d^2}{l^3} \tag{2}$$

Three different surface area densities with the same RD of 0.41 were considered to fill the CC channel of the hot stamping die (Table 4.4). The thickness of the solid skin of the die with a CC channel was decided to be 8 mm, based on the results of independently conducted preliminary study to ensure the proper rigidity (about 64% of solid die stiffness).

Table 4.4. Geometric parameters of the cross lattice structures

Cross structure	RD	Unit cell edge length l (mm)	Strut diameter d (mm)	Surface area density ρ_A (m^{-1})
Case I		6.0	3.0	431.5
Case II	0.41	4.0	2.0	647.2
Case III		2.0	1.0	1294.4

For the mechanical testing and microstructural analysis of the cross lattice structures, bulk cross lattice samples ($24 \times 24 \times 27$ mm^3) were also produced with the same AM process conditions (Fig. 4.5(c)). Quasi-static compression tests of bulk cross lattice samples were performed using a universal testing machine (DTU900-MH, Daekyoung, South Korea) with a constant compressive speed of 1 mm/min at room temperature. The displacement was measured by a laser extensometer (LX 500, MTS, MN, USA). The test was performed at least three times for each surface area density.

4.3.2. Heating and rapid cooling tests

For simplicity of the heating procedure during the experiment, 1180CP ultra-high strength steel (UHSS) sheets were used instead of typical Al-Si coated boron steels. Blanks were prepared from 1.2 mm thick 1180CP UHSS sheets with the length and width of 130 mm and 50 mm, respectively. The blank was set up between the top die with AM lattice structural CC channel and the bottom solid die, as shown in Fig. 4.6. First, the blank was rapidly heated to approximately 925 °C by resistance heating (41.67 kA/mm^2, 5 sec). Then, the heated blank was quickly pressed by the top die against the bottom die within 2.5 sec. The heated blank was finally cooled down between the

top and bottom dies at a constant compressive load of 20 kN for 15 sec to avoid the effect of pressure on the cooling performance. During the cooling period, the flow rate of the coolant (water) was controlled by the flow control valve and measured using a flow meter. During the test, the temperature of the blank was recorded as a function of time using an infrared thermal imaging camera (FLIR-T621, FLIR, Sweden).

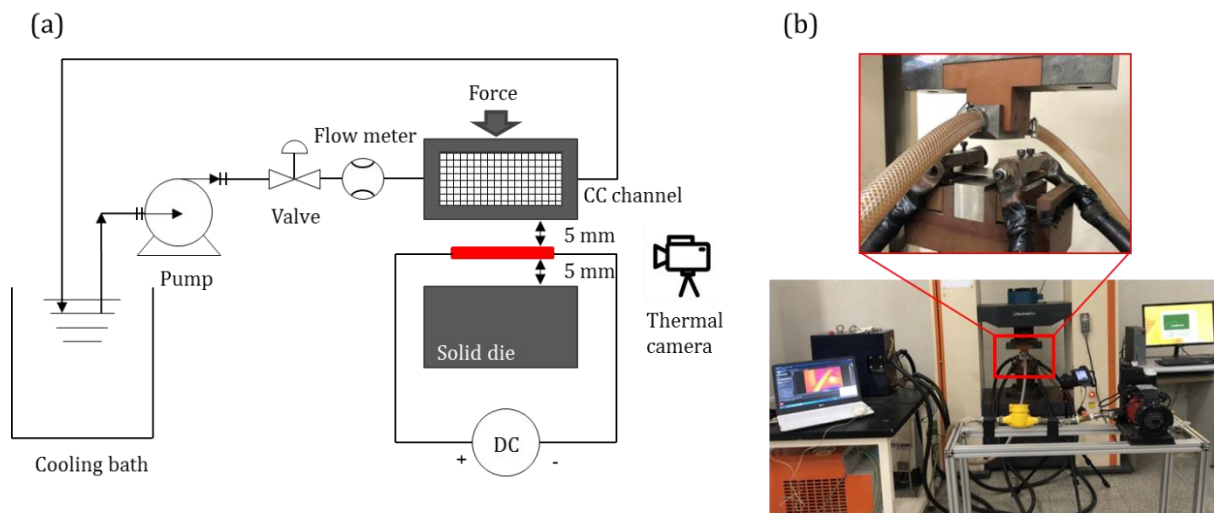**Figure 4.6.** (a) Schematic and (b) the picture of the experimental set-up.

The effect of mass flow rate of coolant on the cooling performance was first evaluated using the case III CC channel die (Table 4.4) with three different flow rates (0, 0.18, and 0.35 kg/s). After that, a constant coolant flow rate of 0.35 kg/s was used to evaluate the cooling performance of different surface area densities.

4.3.3. CFD simulation

The effect of different surface area densities on the cooling performance was also analyzed by CFD to confirm the experimental results. A commercial CFD software (Ansys Fluent 18.2, ANSYS, PA, USA) was employed for geometric modeling, meshing, and calculation. To reduce the calculation time, a quarter of the actual model was adopted with symmetric boundary conditions (Fig. 4.7). Mass flow inlet condition was used for the inlet boundary condition. The mass flow rate was 0.0875 kg/s for a quarter of the inlet mass flow rate, equivalent to 0.35 kg/s of the experimental inlet mass flow rate. The inlet temperature, turbulent intensity, and hydraulic diameter of the inlet flow were 20 $^\circ$C, 5 %, and 0.015875 m, respectively. The outflow condition was adopted as an outlet condition. The temperature of the blank was 900 $^\circ$C. Highly dense meshes were used in the fluid region, especially in the regions that had contact with the die and the lattice structure, as shown in Fig. 4.8 with the basic physical parameters for CFD. The number of elements for each case is shown in Table 4.5. The SIMPLEC algorithm was selected for the pressure-velocity coupling. The equations were solved for a steady model with a pressure-based algorithm. A second-order upwind scheme was adopted for the space discretization of the governing equations.
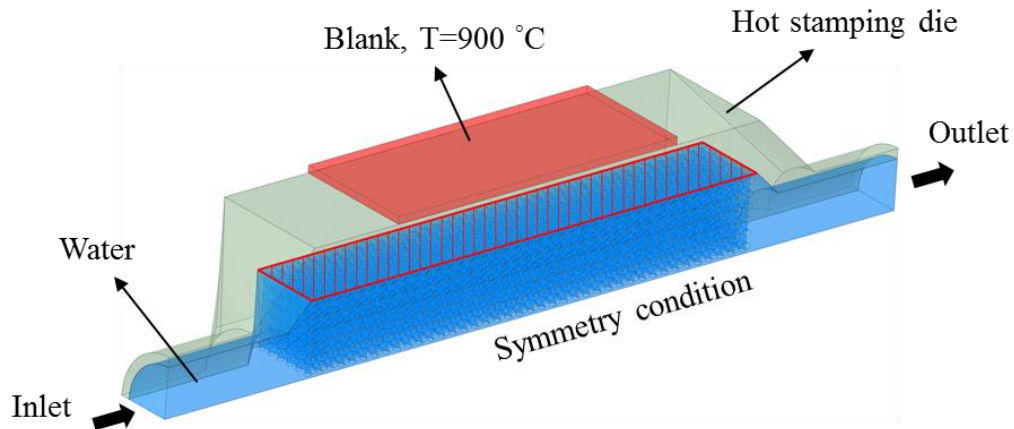
Figure 4.7. Schematics of CFD analysis and boundary conditions.

Materials	Density (g/cm³)	Specific Heat (J/kgK)	Thermal Conductivity (W/mK)	Viscosity (kg/ms)
Blank	8.03	502.48	16.27	-
Die	8.00	465	15	-
Water	0.99	4182	0.6	0.001003

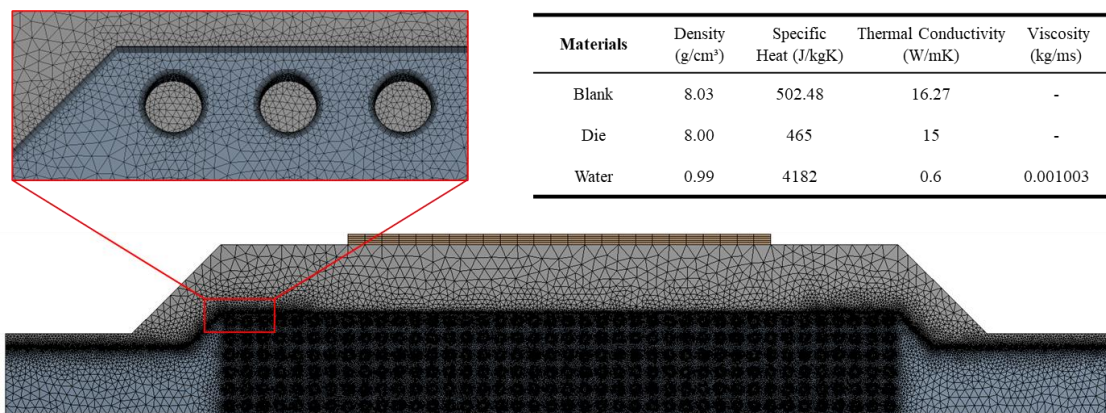**Figure 4.8.** CFD analysis: the mesh structure and material parameters (case III).

Table 4.5. The number of elements for each case of lattice structures

Case	Case I	Case II	Case III
Number of elements	46.182.985	82.411.601	97.236.418

4.4. Results and discussion

4.4.1. AM quality of the lattice structure and mechanical properties

As shown in the optical micrographs of the polished and unetched AMed cross lattice structure specimen (Fig. 4.9), no macroscopic cracks or broken parts were observed in the structure. The AMed cross lattice achieved an average bulk density of 99.5% ± 0.45% which is slightly lower than the bulk sample average density of 99.8% ± 0.2%. Optical microscopy was used to determine density for each cross section of struts and nodes in the lattice structure.
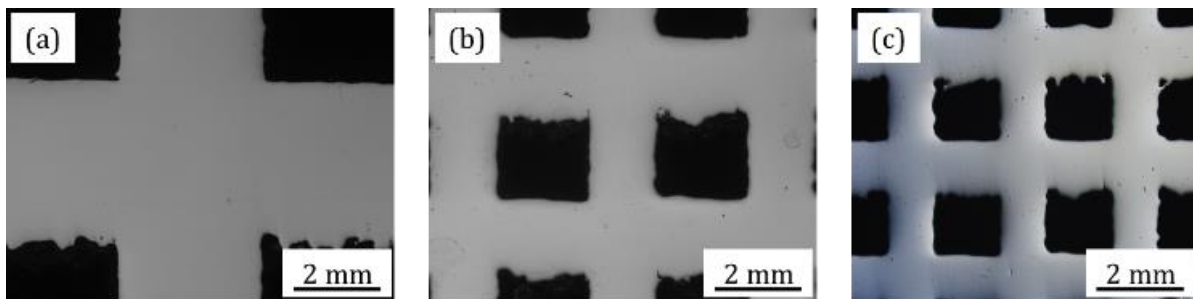

Figure 4.9. Optical micrographs of the cross lattice structure with various surface densities: (a) case I, (b) case II, and (c) case III.

The optical micrograph (Fig. 4.10(a)) of the etched AMed cross lattice structure specimen revealed the morphology of laser melted tracks and melted pools along the build direction (Z-direction). The typical microstructure of AMed material resulted from building a new layer stacked on top of the previous layers. The depths of the melted pools were determined to be in the range of 43 to 65 µm. Scanning electron microscopy (SEM) showed a complex cellular solidification microstructure (Figs. 4.10(b) and (c)). The cellular structure with varying cell growth directions existed in every grain, and the cell size was smaller than 1 µm.
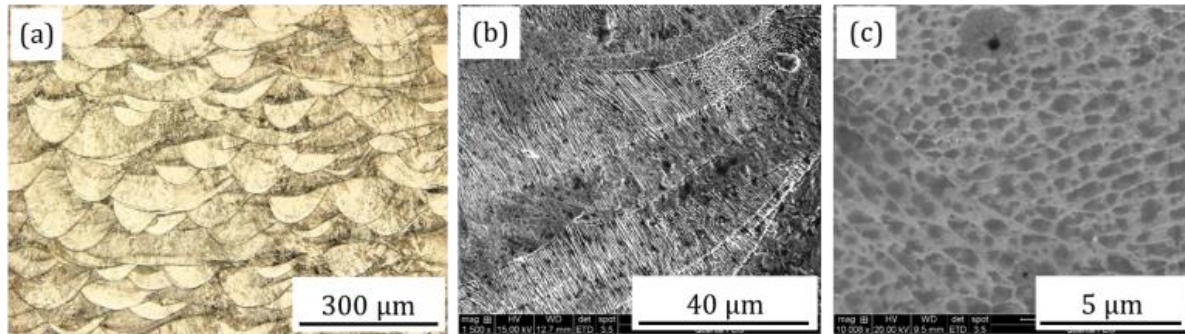
Figure 4.10. (a) Optical micrograph and (b), (c) SEM images of the cross lattice structure in etched condition (case III).

The mechanical properties of lattice structures depend mostly on their RD [14]. Since cross lattice structures with three different surface area densities in the present study (Cases I, II, and III) have the same RD, the same construction, and are made of the same material, their elastic modulus and yield strengths are almost equivalent (Table 4.6). Note that the pressure on the die during a typical hot stamping process is generally lower than 24 MPa [17]. As listed in Table 4.6, the yield strengths of the cross lattice structures were higher than 300 MPa, which are clearly higher than the pressure generally applied to the hot stamping die in service.

**Table 4.6.** Mechanical properties of cross lattice structure samples

	RD	Elastic modulus (GPa)	0.2% Yield stress (MPa)
Case I		23.5±0.8	341±3
Case II	0.41	22.5±0.9	339±2
Case III		22.4±2.9	312±6

4.4.2. The heat transfer performance

The temperature histories of blanks in the heating and rapid cooling tests using the case III CC channel die with three different mass flow rates (0, 0.18, and 0.35 kg/s) were measured as a function of time, as shown in Fig. 4.11. The mass flow rate of 0 kg/s means that there was no water flow running through the lattice CC channel of the upper die. For each flow rate, the experiment was performed at least five times, but only one representative temperature profile for each flow rate is shown for a better presentation. First, the temperature was rapidly increased to approximately 925 $^{\circ}$C by resistance heating in 5 sec (point a). The electric current was then turned off, and the blank began to slowly cool down to about 860 $^{\circ}$C until the upper CC channel die touched the heated blank (point b). From the point b to the point c, the heated blank was pushed down by the upper die until it was compressed against the lower solid die. Once the upper and lower dies completely compressed the heated blank (point c), the coolant flow was turned on, and the heated blank was rapidly quenched with a constant compressive force of 20 kN in 15 sec.

To compare the cooling performance of the lattice structural CC channels, the average cooling rate was calculated in the temperature range from 700 $^{\circ}$C to 400 $^{\circ}$C, as marked in Fig. 4.11. The temperature of 700 $^{\circ}$C corresponds to the moment (point c) when the heated blank began to be cooled down by the heat transfer induced by the coolant flow through the lattice structural CC channel. Also, the lower bound for the calculation of the average cooling rate was selected to be 400 $^{\circ}$C, which is the martensite transformation starting temperature [18].

For the water flow rate of 0 kg/s (no water flow), the blank was quenched with an average cooling rate of 37.91 $^{\circ}$C/s. As the mass flow rate increased to 0.18 kg/s and 0.35 kg/s, the cooling rate of the blank increased by 29.2% (48.99 $^{\circ}$C/s) and 95.7%, (74.20 $^{\circ}$C/s), respectively. Note that the acceptable cooling rate for the commercial hot stamping process is about 27 $^{\circ}$C/s [18].

92
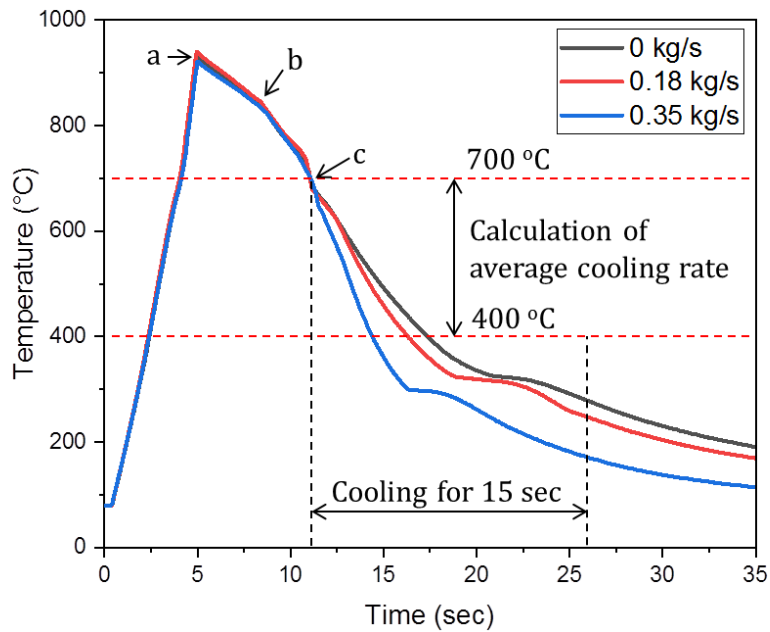
a: End of heating; b: The top die begins to touch the heated plank;
c: Quenching by the coolant flow through the CC channel

Figure 4.11. Temperature histories of the blank quenched with three different mass flow rates (case III).
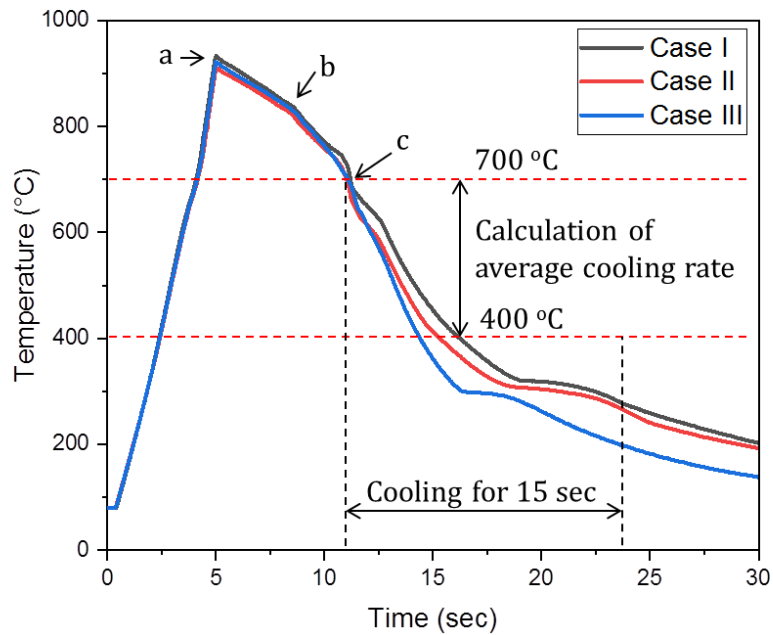

Figure 4.12. The temperature histories of blank quenching with three surface area densities at the same mass flow rate of 0.35 kg/s.

With the identical RD, the lattice structural CC channels with different surface area densities resulted in different cooling rates for the same mass flow rate of 0.35 kg/s (Fig. 4.12). As the surface area density increased, the cooling rate increased, as summarized in Fig. 4.13. This result clearly confirms that the cooling performance of a lattice structural CC channel can vary significantly for the same RD of the lattice structure. Therefore, the heat transfer design of the lattice structural CC channel should be based on the surface area density rather than the RD. In this way, while designing the mechanical properties of the lattice structure based on the RD to a satisfactory level, the heat transfer efficiency can be improved by adjusting the surface area density of the structure.

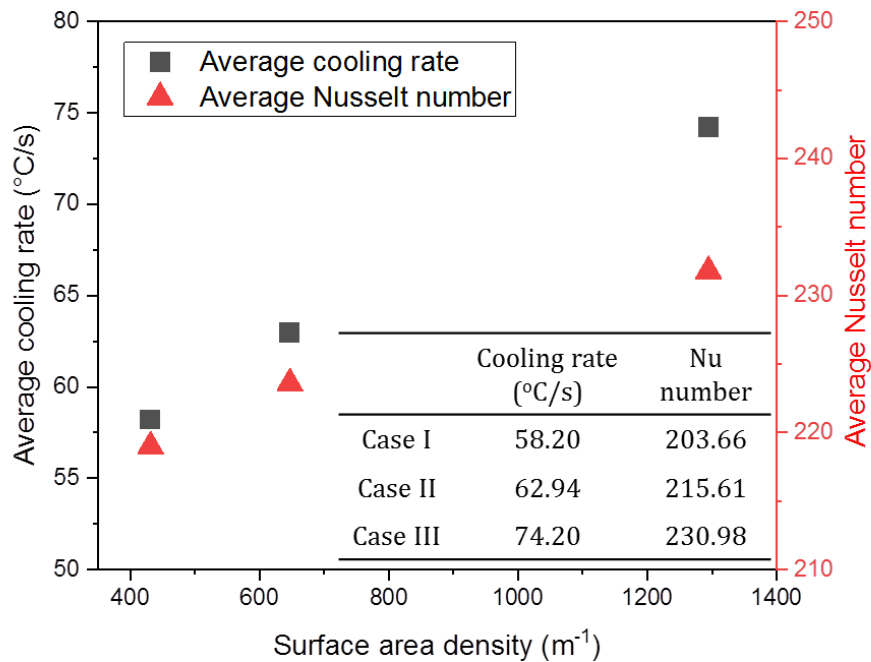|	Cooling rate (°C/s)	Nu number
Case I	58.20	203.66
Case II	62.94	215.61
Case III	74.20	230.98

Figure 4.13. The average cooling rate of blank and average Nusselt number as functions of surface area density of lattice structure.

4.4.2. CFD analysis

During the cooling process, heat is mostly dissipated through the cooling channel by heat convection. The Nusselt number is an essential non-dimensional parameter to represent the ratio of convective heat transfer to conduction, which means that a larger Nusselt number enhances cooling performance with a larger convective heat transfer coefficient. The Nusselt number Nu is calculated by equations (3) [19],

$$Nu = \frac{hL}{k} = \frac{qL}{k(T-T_{in})}$$ (3)

where h is the convective heat transfer coefficient, $L = V_l/A_l$ is the characteristic length (V_l: the volume of lattice structure zone, A_l is the area of lattice structure zone), k is the thermal conductivity of water, T is the local temperature, $q = d\dot{Q}/dA$ is the heat flux ($\dot{Q}$: the overall heat transfer rate). Values of the Nusselt number in the range from 1-10 are characteristic of laminar flow [16]. A larger Nusselt number indicates more active convection with turbulent flow, typically in the 100-1000 range [19].

Simulation results show that the average Nusselt number increases as the surface area density of the lattice structure increases (the inset of Fig. 4.13), thus clearly confirming the experimental result. The increasing Nusselt number with increasing surface area density of the lattice structure also suggests that the water flow became more turbulent with increasing surface area density, which further assists a higher heat transfer efficiency.

Figure 4.14 shows the velocity vectors of the coolant flow in the CC channel with different surface area densities at the mass transfer rate of 0.35 kg/s. The cross lattice structure disturbed

the inlet flow, established a turbulent flow, and generated local vortex regions [20]. The maximum flow velocity of coolant was much higher than the inlet flow rate, while the maximum flow velocity in the three cases was similar. Moreover, as the surface area density increased, the number of generated vortices and high-speed flows increased. Accordingly, the heat transfer efficiency of the lattice CC channel significantly increased as the surface area density increased [12].
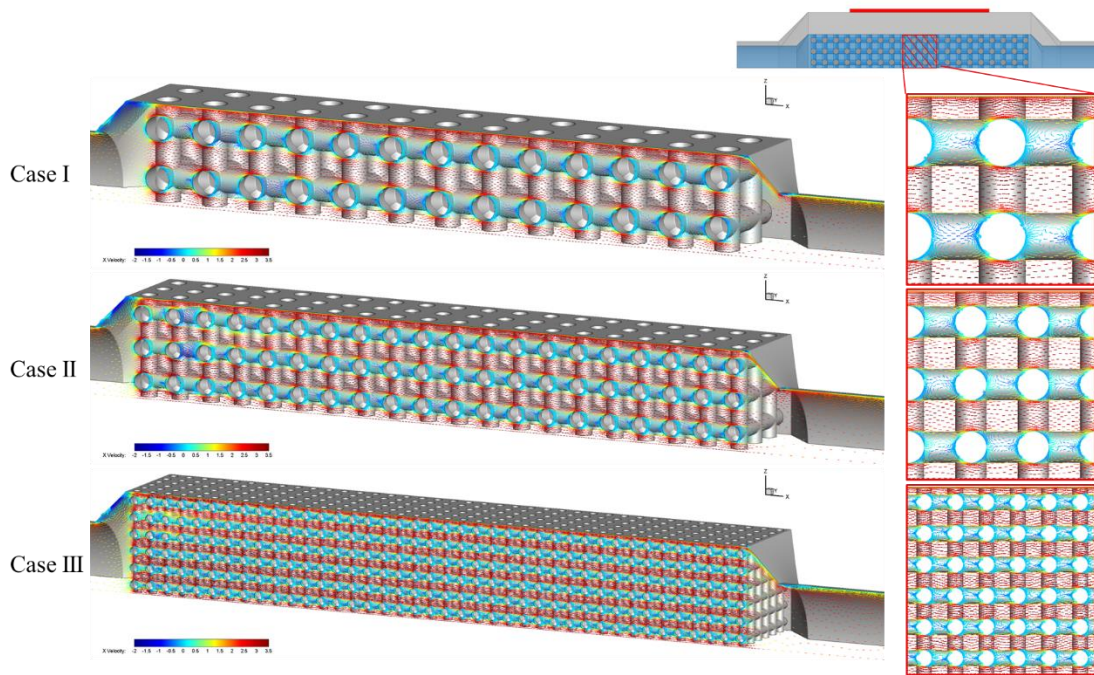

Figure 4.14. The velocity vector of the coolant flow with different surface area densities.
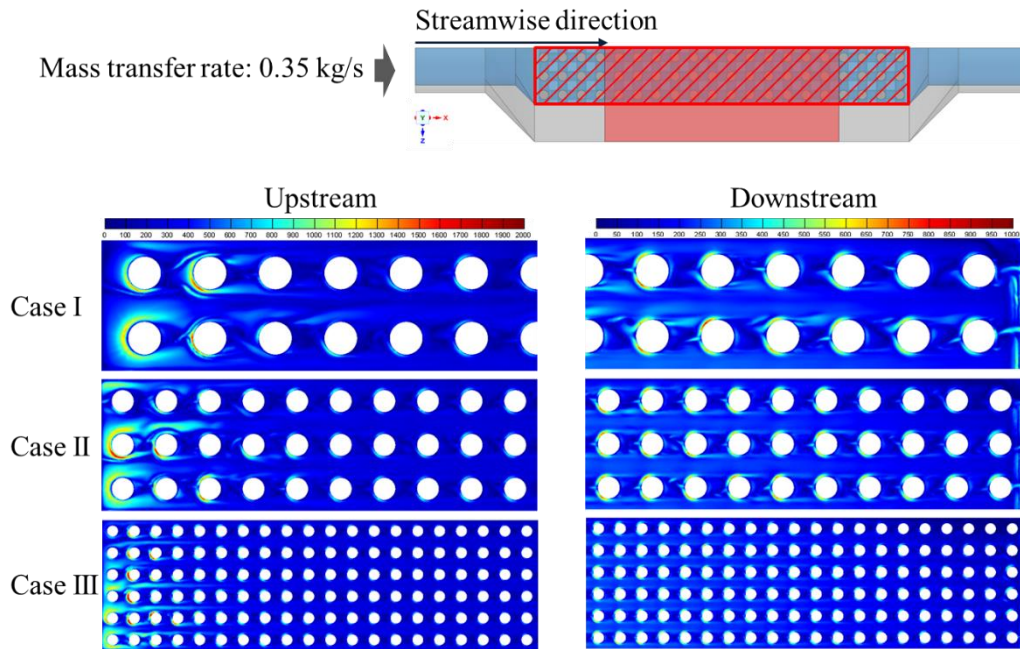
Figure 4.15. Nusselt number contour with different surface area densities.

Figure 4.15 shows the Nusselt number contour on the surface of CC channels with different surface area densities at the inlet mass transfer rate of 0.35 kg/s. According to the simulation results, the Nusselt number decreased gradually from upstream to downstream of the coolant flow. That is due to the fact that the pressure decreased as the coolant entered through the spaces of the lattice structure [21]. Also, for the cross lattice structure in the present study, with increasing surface area density, the distance between the adjacent struts of structure narrowed, resulting in a reduction of the mean thickness of the boundary layer around the struts (Fig. 4.15). Therefore, with increasing surface area density, both the heat transfer coefficient and the heat transfer area increase.

4.5. Conclusions

In this study, the cooling performance of the lattice CC channel produced by the metal AM process was investigated for hot stamping. Experimental tests accompanied by CFD simulation were performed to evaluate cooling performance and fluid flow analysis of the lattice CC channel with respect to surface area density. As the inlet velocity increased, the cooling rate of the blank increases significantly. As shown in the experimental results and confirmed by the CFD analysis, increasing the surface area density of the lattice structure can lead to improved cooling performance by about 27.5% without altering the mechanical properties of the forming die, which are based on the RD of the structure. The cooling efficiency in the hot stamping process dramatically affects the efficiency of the entire process and resultant manufacturing cost. Therefore, the proper design of a rapid cooling die will contribute to the development of a cost-effective and efficient advanced hot stamping process.

References

[1] Karbasian H, Tekkaya AE, A Review on Hot Stamping. Journal of Materials Processing Technology (2010), 210(15):2103–2118.

[2] H. Hoffmann, H. So, H. Steinbeiss, Design of hot stamping tools with cooling system, CIRP Ann. Manuf. Technol. 56 (2007), 269–272.

[3] P. Zhu, P. Hu, Y. Liu, X. Zhao, M. Ding, M. Zhou, Topology optimization of channel cooling structures considering thermomechanical behavior, Struct. Multidiscip. Optim., 59 (2018), pp. 613–632.

[4] S.N.A. Shahbudin, M.H. Othman, S.Y.M. Amin, M.H.I. Ibrahim, A review of metal injection molding- Process, optimization, defects and microwave sintering on WC-Co cemented carbide IOP Conf. Ser. Mater. Sci. Eng., 226 (2017), Article 012162.

[5] E. Sachs, E. Wylonis, S. Allen, M. Cima, H. Guo (2000) Production of Injection Molding Tooling With Conformal Cooling Channels Using the Three Dimensional Printing Process, Polymer Eng. And Sci, Vol. 40.

[6] M. Mazur, P. Brincat, M. Leary, M. Brandt (2017) Numerical and experimental evaluation of a conformally cooled H13 steel injection mould manufactured with selective laser melting. Int. J. Adv. Manuf. Technol., 93, pp. 881–900.

[7] Ngo TD, Kashani A, Imbalzano G, Nguyen KTQ, Hui D (2018) Additive manufacturing (3D printing): A review of materials, methods, applications and challenges. Compos Part B Eng 143: 172–196.

[8] H. Liu, C. Lei, Z. Xing (2013) Cooling system of hot stamping of quenchable steel BR1500HS: optimization and manufacturing methods, Int. J. Adv. Manuf. Technol. 69 211–223.

[9] T. Wu, S.A. Jahan, Y. Zhang, J. Zhang, H. Elmounayri, A. Tovar (2017) Design optimization

of plastic injection tooling for additive manufacturing, Procedia Manuf. 10, 923–934.

[10] S.A. Jahan, T. Wu, Y. Zhang, H. El-Mounayri, A. Tovar, J. Zhang, D. Acheson, R. Nalim, X. Guo, W.H. Lee (2016) Implementation of conformal cooling & topology optimization in 3D printed stainless steel porous structure injection molds, Procedia Manuf. 5, 901–915.

[11] K.N. Son, J.A. Weibel, V. Kumaresan, S.V. Garimella (2017) Design of multifunctional lattice-frame materials for compact heat exchangers, Int. J. Heat Mass Transf. 115, 619–629.

[12] S. Yun, J. Kwon, D.C. Lee, H.H. Shin, Y. Kim (2020). Heat transfer and stress characteristics of additive manufactured FCCZ lattice channel using thermal fluid-structure interaction model, Int. J. Heat Mass Transf. 149 119187.

[13] K.M. Au, K.M. Yu (2007) A scaffolding architecture for conformal cooling design in rapid plastic injection moulding, Int. J. Adv. Manuf. Technol. 34, 496–515.

[14] L.J. Gibson, M.F. Ashby (1997) Cellular Solids: Structure and Properties, Cambridge university press.

[15] S.-T. Hong, & D. R. Herling (2006) Open-cell aluminum foams filled with phase change materials as compact heat sinks. Scripta Materialia, 55(10), 887–890.

[16] Moore, M. (1974) Symmetrical Intersections of Right Circular Cylinders, Math. Gaz. 58, 181-185.

[17] Carob, E. J. F. R., Daun, K. J., Well, M. A. (2014) Experimental heat transfer coefficient measurements during hot forming die quenching of boron steel at high temperatures. International Journal of Heat and Mass Transfer, 71, 396–404.

[18] M. Merklein, J. Lechler, M. Geiger (2006) Characterisation of the Flow Properties of the Quenchenable Ultra High Strength Steel 22MnB5, CIRP Annals - Manufacturing Technology, Volume 55, Issue 1, Pages 229–232.

울산대학교
UNIVERSITY OF ULSAN

[19] F. P. Incropera, D. P. DeWitt (2001) Fundamentals of Heat and Mass Transfer, 5th Edition, Wiley.

[20] K.N. Son, J.A. Weibel, V. Kumaresan, S.V. Garimella Design of multifunctional lattice-frame materials for compact heat exchangers Int. J. Heat Mass Transf., 115 (2017), pp. 619–629.

[21]   S.W. Hwang, D.H. Kim, J.K. Min, J.H. Jeong, CFD analysis of fin tube heat exchanger with a pair of delta winglet vortex generators, J. Mech. Sci. Technol., 26 (2012), pp. 2949–2958.

CHAPTER V

CONCLUSIONS

In conclusion, the use of lattice structures in design for additive manufacturing (DfAM) is a significant development in both technical design and production. By taking advantage of AM technology's unique characteristics, designers may develop previously unattainable creative, lightweight, and high-performance components. The use of DfAM with lattice structures is anticipated to grow as research and development in this field advances, spurring efficiency and innovation across a range of industries, such as aerospace, medical implants, automotive industry. So, the study aims to understand the mechanical properties of structures manufactured using AM methods with differences in base materials, unit cell sizes, and relative densities. The findings provide practical guidelines for DfAM using lattice structures, particularly those requiring tailored energy absorption and cooling performance.

The major achievements/findings of this dissertation can be summarized as follows:

- In DfAM with lattice structures, the angle at which a cell is printed can affect its success because it influences the amount and placement of supports required. Often, a structure can be rotated to increase manufacturing capabilities.

- By examining stainless steel 316L, tool steel 1.2709, titanium alloy (Ti-Gr.2), and aluminum alloy (AlSi10Mg) lattice structures under compressive load, the research identifies significant variations in compressive failure modes based on relative density. Specifically, Low relative densities show a layer-by-layer collapse, whereas greater densities show a bulk failure mechanism. Furthermore, the Gibson-Ashby model offers a significant breakthrough in forecasting the performance of these lattice structures at

various relative densities. The findings of this work not only improve our understanding of material behavior in AMed lattice structures but also provide practical advice for enhancing the design and functionality of AM components. Engineers and designers can use these discoveries to improve efficiency, reliability, and performance in a variety of engineering applications, particularly those that require specialized energy absorption.

- The design principle of an additively manufactured (AMed) lattice structural conformal cooling channel for hot stamping is investigated. Through a combination of experimental tests and CFD simulations, the study highlights the important impact of surface area density on cooling performance and fluid flow in lattice CC channels. The findings demonstrate that increasing the inlet velocity significantly enhances the cooling rate of the workpiece. Furthermore, optimizing the surface area density of the lattice structure can improve the cooling efficiency by about 27.5% without affecting the mechanical properties of the forming die. The improved cooling efficiency observed in this study underscores the potential for significant advancements in the hot stamping process. Enhanced cooling rates directly contribute to increased process efficiency and reduced manufacturing costs, making the design of a rapid cooling die a crucial factor in the development of cost-effective and efficient hot stamping technologies. By adopting these optimized lattice structures based on surface area density, manufacturers can achieve better thermal management, leading to higher-quality products and more efficient production cycles.